© 2020. Published by The Company of Biologists Ltd | Journal of Cell Science (2020) 133, jcs250241. doi:10.1242/jcs.250241

RESEARCH ARTICLE

# Mitochondria control mTORC1 activity-linked compartmentalization of eIF4E to regulate extracellular export of microRNAs

**Susanta Chatterjee[§], Yogaditya Chakrabarty[*,§], Saikat Banerjee[§], Souvik Ghosh[‡,§] and Suvendra N. Bhattacharyya[¶]**

## ABSTRACT

Defective intracellular trafficking and export of microRNAs (miRNAs) have been observed in growth-retarded mammalian cells having impaired mitochondrial potential and dynamics. Here, we found that uncoupling protein 2 (Ucp2)-mediated depolarization of mitochondrial membrane also results in progressive sequestration of miRNAs within polysomes and lowers their release via extracellular vesicles. Interestingly, the impaired miRNA-trafficking process in growth-retarded human cells could be reversed in the presence of Genipin, an inhibitor of Ucp2. Mitochondrial detethering of endoplasmic reticulum (ER), observed in cells with depolarized mitochondria, was found to be responsible for defective compartmentalization of translation initiation factor eIF4E to polysomes attached to ER. This caused a retarded translation process accompanied by enhanced retention of miRNAs and target mRNAs within ER-attached polysomes to restrict extracellular export of miRNAs. Reduced compartment-specific activity of the mammalian target of rapamycin complex 1 (mTORC1), the master regulator of protein synthesis, in cells with defective mitochondria or detethered ER, caused reduced phosphorylation of eIF4E-BP1 and prevented eIF4E targeting to ER-attached polysomes and miRNA export. These data suggest how mitochondrial membrane potential and dynamics, by affecting mTORC1 activity and compartmentalization, determine the subcellular localization and export of miRNAs.

**KEY WORDS: miRNA, Processing bodies, P-body, Mitochondria, Polysome, Extracellular vesicles, Exosomes, eIF4E, mTORC1**

## INTRODUCTION

MicroRNAs (miRNAs) are small 20–24-nucleotide-long non-coding RNAs that post-transcriptionally regulate the expression of their cognate mRNAs by base pairing, and thereby regulate majority of genes in higher animals and plants (Bartel, 2009). Interestingly, cellular structures and organelles also play important roles in controlling the activity of miRNAs. It has been shown that miRNA-mediated repression and target RNA degradation are both temporally and spatially uncoupled processes (Bose et al., 2017). The process starting from biogenesis of a miRNA through to silencing of target mRNAs requires the involvement of various cellular organelles, as they serve as destinations of miRNAs and respective target mRNAs under specific phases of target repression (Barman and Bhattacharyya, 2015; Chakrabarty and Bhattacharyya, 2017; Gibbings et al., 2009; Li et al., 2013).

miRNAs function in the form of ribonucleoprotein complexes called miRNA-induced silencing complexes (miRISCs). Components of miRISCs and repressed mRNAs are also enriched in P-bodies – specialized structures for mRNA storage and degradation (Eulalio et al., 2007; Parker and Sheth, 2007). The concept of P-body involvement in an mRNA storage function has been strengthened in a recent report where the authors have identified several miRNA-targeted mRNAs in biochemically purified P-bodies (Bhattacharyya et al., 2006; Hubstenberger et al., 2017).

Mitochondrial membrane potential not only helps production of ATP through oxidative phosphorylation but it is also involved in regulation of miRNA activity. Interestingly, mitochondrial membrane potential disruption has implication in the miRNA-mediated repression process (Ernoult-Lange et al., 2012) and it has been shown that mitochondrial membrane potential is required for endoplasmic reticulum (ER) and endosome tethering of mitochondria, which in turn controls miRNA activity in mammalian cells (Chakrabarty and Bhattacharyya, 2017). The ER has been reported as sites of miRISC-mediated target RNA recognition and *de novo* miRNA ribonucleoprotein (miRNP) complex formation (Barman and Bhattacharyya, 2015; Bose et al., 2020) while Multivesicular bodies (MVBs), which interact with RNA processing bodies, are important sites for target RNA degradation (Bose et al., 2017). Additionally, MVBs or late endosomes can merge with the plasma membrane to export various cargoes through the formation of extracellular vesicles (EVs) known as exosomes. These lipid bilayer sequestered bodies are small, 30- to 100-nm sized, EVs considered as a primary means of intercellular communication (Hunter et al., 2008; Simons and Raposo, 2009; Théry et al., 2002; van Niel et al., 2018). Many miRNAs along with their associated proteins, such as Ago2 and GW182B (also known as TNRC6B), are reported to be present in exosomes or EVs (Valadi et al., 2007). As of yet, the significance of miRNA export via EVs and its regulation, in addition to their role as an intercellular signaling factor for the maintenance of cellular homeostasis, is only partly understood (Ghosh et al., 2015; Mukherjee et al., 2016).

Mammalian target of rapamycin (mTOR) plays a crucial role in controlling mitochondrial metabolism. Inhibition of mTOR activity leads to reduced mitochondrial respiration and enhanced aerobic glycolysis (Ramanathan and Schreiber, 2009). Another observation suggests that mTOR complex 1 (mTORC1) stimulates mitochondrial biogenesis and activity and translation of mitochondria-related mRNAs, mediated by eIF4E-binding proteins (eIF4E-BPs) (Morita

RNA Biology Research Laboratory, Molecular Genetics Division, CSIR-Indian Institute of Chemical Biology, Kolkata 700032, India.
*Present address: Broad Center for Biological Sciences, Division of Biology and Biological Engineering, California Institute of Technology, Pasadena, CA 91106, USA.
‡Present address: Biozentrum, University of Basel, Klingelbergstrasse 50/70, 4056 Basel, Switzerland.
§These authors contributed equally to this work

¶Author for correspondence (sb@csiriicb.in; suvendra@iicb.res.in)

S.C., 0000-0003-0396-2670; Y.C., 0000-0002-3230-9251; S.G., 0000-0003-4152-4460; S.N.B., 0000-0001-9697-3824

**Handling Editor: Jennifer Lippincott-Schwartz**
**Received 16 June 2020; Accepted 17 November 2020**

Journal of Cell Science (2020) 133, jcs250241. doi:10.1242/jcs.250241

et al., 2013). In reverse, how mitochondrial dysfunction influences mTORC1 activity to regulate cellular translational and miRNP machineries or their trafficking remain to be understood.

We report here that depolarization of mitochondria and their reduced dynamics, as observed in growth-arrested cells, is functionally coupled to retardation of movement of miRNPs from polysomes to MVBs. This happens in conjunction with uncoupling protein 2 (Ucp2)-dependent mitochondrial depolarization and subsequent accumulation of miRNAs on polysomes, which in turn causes reduced exosomal miRNA export and P-body targeting of Ago proteins. Interestingly, reduced mTORC1 activity-driven defective compartmentalization of translation initiation factor eIF4E to polysomes attached to the rough ER (rER) membrane causes the retarded translation of protein, which in turn abrogates intracellular shuttling and subsequent export of miRNAs in mammalian cells.

## RESULTS

### Reduced mitochondrial dynamics in growth-retarded mammalian cells

Previously, we have explored the status of miRNA machineries in cells that are growth retarded. These growth-retarded high-density culture (HDC) cells are morphologically and biochemically different from the proliferating low-density culture (LDC) cells (Ghosh et al., 2015). To investigate the cause of the defective miRNA metabolism happening in the HDC cells, we have explored the status of energy metabolism in both HDC and LDC cells to determine its importance in defective miRNP machineries observed in HDC cells. In mammalian macrophages, and also in non-macrophage cells, mitochondrial detethering from the ER causes increased miRNA stability, which is also observed in HDC cells (Chakrabarty and Bhattacharyya, 2017; Ghosh et al., 2015).

To ascertain the effect of growth status on mitochondrial morphology and activity in human cells, HeLa and MDA-MB-231 cells were grown separately as LDC (25–40%) and HDC (100%) states. For assessing the mitochondrial status, the cells were transfected with a mitochondria-targeting GFP (Mito-GFP) and an ER-targeting variant of DsRed2 (DsRed2-ER) and were studied microscopically. Evidently, a significant variation in shape and structure of mitochondria between HDC and LDC state cells was observed. In the LDC condition, mitochondria appear as long filamentous structures whereas, in the HDC condition they are predominantly punctate and spherical (Fig. 1A; Fig. S1A). Moreover, when we quantified the length of individual mitochondrial filaments using 3D surface reconstructions of the confocal images taken for both LDC and HDC HeLa as well as MDA-MB-231 cells, we observed a mean length of ∼6 µm in the HDC condition as compared to ∼20 µm long mitochondrial filaments in LDC cells (Fig. 1A,B; Fig. S1B). To connect the effect of this structural change of mitochondria to its dynamics in growth-retarded cells, we explored the spatial dynamics of mitochondria and ER organelles in both HDC and LDC cells by live-cell imaging of the events. The spatial dynamics of mitochondrial structures of LDC cells was clearly different from that of HDC cells. While mitochondria in LDC cells showed fast dynamic and frequent interactions with ER, along with active mitochondrial fusion and fission in LDC cells, mitochondria from HDC cells showed rather a ‘sluggish’ dynamics and appeared as more punctate structures with negligible amount of mitochondrial fusion or overlap with ER (Fig. 1C,D; Fig. S1C, Movies 1–4).

The structural alterations that we observed with the mitochondria of HDC or growth-retarded cells could be due to a possible depreciation in inter-mitochondrial exchange happening specifically in HDC-state cells (Fig. S1D). We performed FRAP-based analysis in LDC and HDC cells. The FRAP-based analysis was utilized as a way to reconfirm the effects of cell densities on mitochondrial dynamics, and we observed effects of cell growth status on mitochondrial exchange dynamics in human cells. The FRAP recovery rate of Mito-GFP in HDC cells was about half of that seen in LDC cells, depicting a functional loss of mitochondrial dynamics and reaffirming the data we obtained for mitochondrial length shortening in HDC cells (Fig. 1E). FRAP experiments were done with portions of mitochondria that formed higher orders of mitochondrial networks; specific branches of a mitochondrion were bleached and checked for recovery in consecutive frames. We identified mitochondria with defined morphology and selectively photo-bleached the region of interest to address the FRAP recovery rates for HDC and LDC cell mitochondria, and measured fluorescence recovery of Mito-GFP in the defined part of the mitochondria (Fig. S1D, Movies 5,6).

### Reduced mitochondrial membrane potential in growth-retarded cells

Mitochondrial membrane potential ($\Delta\Psi_M$) modulation is integrally linked with changes in the structural and movement dynamics of mitochondria (Labbé et al., 2014). Therefore, it was essential to check the effect of cell density on the $\Delta\Psi_M$ in LDC and HDC cells. Altered binding of the dye JC-1 with polarized mitochondria can be used to measure the change in $\Delta\Psi_M$ due to increase in cellular density. A reduction in $\Delta\Psi_M$ was observed in HDC cells compared to LDC state cells. The depreciation in $\Delta\Psi_M$ was substantial (Fig. 1F). The oxygen consumption rate (OCR) measurement reflects a sensitive and dynamic measure of the changes occurring in $\Delta\Psi_M$. OCR-based measurement of $\Delta\Psi_M$ is an excellent method of monitoring active variations in mitochondrial functional state (Brand and Nicholls, 2011). A distinct elevation in the OCR in HDC condition HeLa cells, as well as MDA-MB-231 cells, was observed reflecting a lowered $\Delta\Psi_M$ in HDC state cells (Fig. 1G). Ucp2 is an endogenous mitochondrial uncoupler that is ubiquitously present across different tissues, and we found increased expression of this protein in HDC state cells. As reported before (Chakrabarty and Bhattcharyya, 2017), the increased expression of Ucp2 therefore could account for the lower $\Delta\Psi_M$ observed in HDC state cells (Fig. 1H).

### Mitochondria depolarization caused by FCCP leads to accumulation of miRNAs and Ago2

It has been shown previously that mitochondrial depolarization and detethering from ER caused by the pathogen *Leishmania* is associated with increased accumulation of miRNPs in host macrophages (Chakrabarty and Bhattacharyya, 2017). We have observed a similar increase in miRNP content in HDC stage cells which also have depolarized mitochondria. Therefore, to establish a causal relationship between mitochondrial depolarization and miRNP accumulation, it was important to check the fate of the miRNPs upon induced depolarization of mitochondria. We used a specific chemical blocker of $\Delta\Psi_M$, FCCP, to dissect the effect of $\Delta\Psi_M$ reduction on miRNA activity and stability. FCCP treatment resulted in a robust loss of $\Delta\Psi_M$ in mitochondria from treated cells, as measured by JC-1-based flow cytometry assays (Fig. 2A). Furthermore, when we used FCCP to depolarize mitochondria of HeLa cells, a large increase in the miRNA levels were observed as evidenced by the qRT-PCR based quantification of mature let-7a or miR-21 miRNAs in HeLa cells (Fig. 2B, left). An increased level of the exogenously expressed liver-specific miRNA-122 in HeLa cells was also noted with progressive FCCP treatment (Fig. 2B, right).

Journal of Cell Science (2020) 133, jcs250241. doi:10.1242/jcs.250241

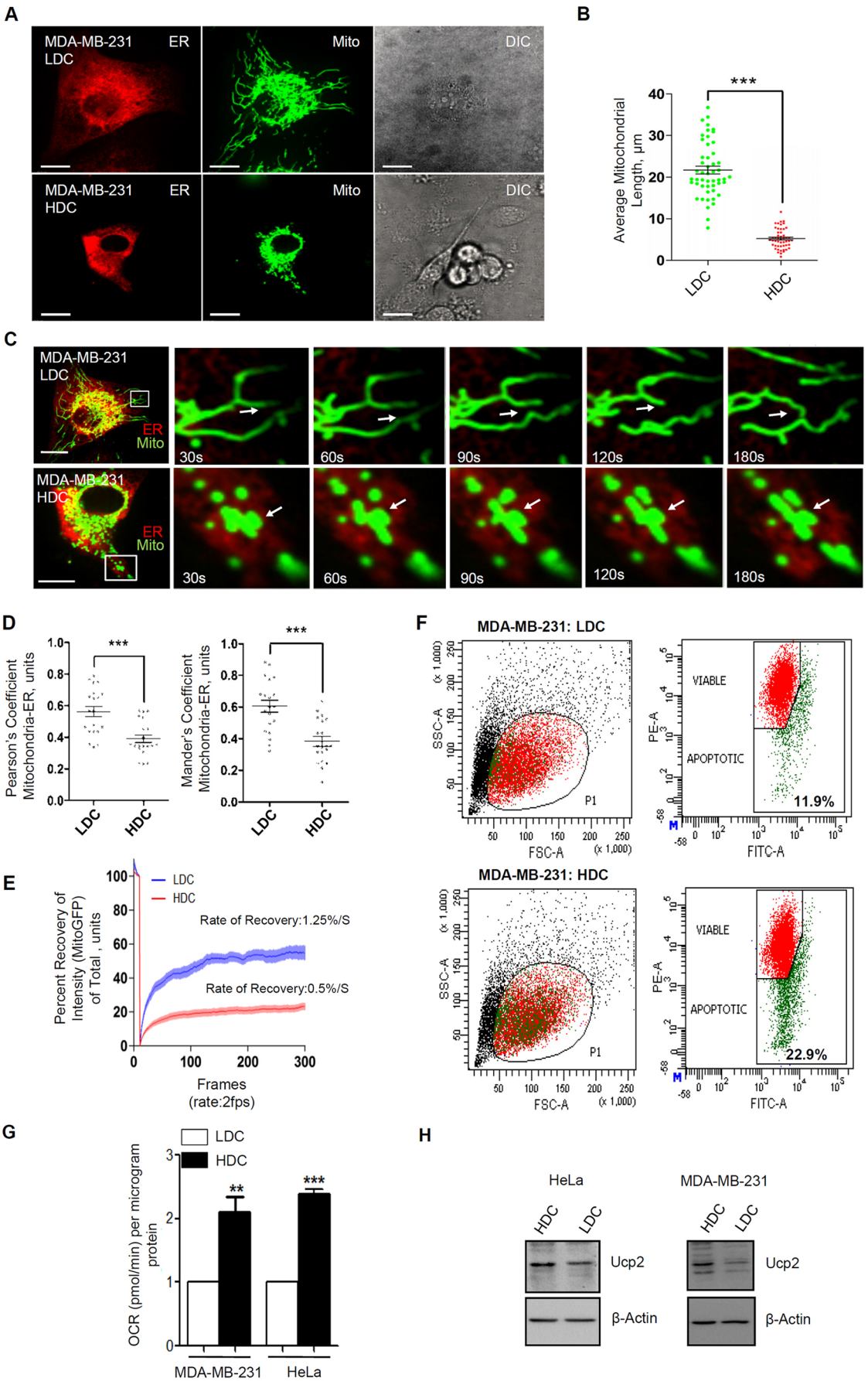


**Fig. 1.** See next page for legend.

Journal of Cell Science (2020) 133, jcs250241. doi:10.1242/jcs.250241

**Fig. 1. Alteration in mitochondrial morphology, dynamicity and membrane potential in growth-retarded mammalian cells.**
(A) Representative pictures of MDA-MB-231 HDC and LDC state cells showing ER and mitochondrial structures. Cells expressing a mitochondrial targeting variant of GFP (MT-GFP, green) and an ER targeting variant of DsRed (pDsRed2-ER, red) were used. Scale bars: 10 µm. (B) Mitochondrial size quantifications (mean±s.e.m.) were performed for LDC or HDC MDA-MB-231 cells. (C) Representative frames of LDC or HDC MDA-MB-231 cells imaged live. Microscopy was performed for a total of 3 mins at 1 fps. Cells expressing a mitochondrial targeting variant of GFP (MT-GFP, green) and an ER-targeting variant of DsRed (pDsRed2-ER, red) were used. Arrows highlight mitochondrial structures, dynamics of which are followed in the timecourse experiments. Scale bars: 10 µm. The ROI as depicted is 10× zoomed. Also see Movie 1 and 2. (D) Pearson's (left) and Mander's (right) coefficients of mitochondria–ER colocalization in HDC and LDC cells. Calculation based on the images taken with cells described in C. (E) FRAP analysis of GFP-positive mitochondria in HDC or LDC MDA-MB-231 cells. Cells expressing a mitochondria-targeting variant of GFP (MT-GFP, green) were used. FRAP analysis was from 100 cells ($n$>4) for indicated experimental sets. MT-GFP was photobleached and images were acquired at 2 fps for 300 frames. The mean intensity values of different regions of interest (ROI) thus obtained was fitted on a scale of 0 to 100. Mean intensity level of designated ROI before bleaching step taken as 100, and the value of mean intensity in ROI just after photobleaching serves as 0. The values were plotted for a total of 300 frames. Shown are the mean±s.e.m. for $n$>20. Fluorescence recovery rates are noted. (F) Representative plots depicting flow cytometry-based quantification of JC-1-stained HDC or LDC HeLa cells. The percentage of cells in the zone with low JC-1 Fluorescence (green) were measured and shown as depicted. (G) Oxygen consumption rate (OCR) determination in HDC and LDC HeLa cells. Quantification of OCR in HDC or LDC MDA-MB-231 and HeLa cells from five different experiments (mean±s.e.m.). (H) Representative western blot analysis of Ucp2 protein level in HDC or LDC HeLa or MDA-MB-231 cells. β-Actin served as loading control protein. **$P$<0.01, ***$P$<0.001 (Student's $t$-test).

Furthermore, the *in vitro* target cleavage activity of the miR-122-containing FLAG–HA–Ago2 miRISC purified from HeLa cells co-expressing miR-122 and FLAG–HA–Ago2 was measured. miRISC from FCCP-treated cells showed elevated activity, which is consistent with the increased stabilization and Ago2 association of the miR-122 mimic, as observed in HDC state cells (Fig. 2C,D). As would be expected, previous studies have depicted the involvement of cellular organelles like rER in controlling miRNA life cycle (Barman and Bhattacharyya, 2015; Bose et al., 2020; Ghosh et al., 2015; Stalder et al., 2013). We checked the association of miRNPs with biochemically isolated rough ER fragments, the microsomes, in control and FCCP-treated cells. As evident from the measurement of amount of Ago2 protein fractionated with the microsomes, FCCP treatment increased the amount of Ago2 in microsome fractions (Fig. 2E). To ascertain a more specific subcellular structure for where the miRNP increase was occurring in FCCP-treated cells, an Optiprep®-based gradient was used for separation of cellular organelles (Bose et al., 2020). Measurement of miRNA levels in individual fractions suggest elevated association of let-7a in the fractions known to be enriched for ER (Bose et al., 2020) upon FCCP treatment, as was observed in HDC stage cells or in cells expressing Ucp2 exogenously (Chakrabarty and Bhattacharyya, 2017; Ghosh et al., 2015) (Fig. S2A,B).

### Reduced EV-mediated export of miRNAs in cells with depolarized mitochondria

Increased retention of miRNAs with the polysomes, observed in HDC state cells, can be contributed to by reduced mitochondrial activity and membrane potential. To test the fate of miRNAs in cells with depolarized mitochondria, the levels of miRNAs associated with polysomes was measured in HeLa cells expressing a FLAG- and HA-tagged version of Ucp2 (FH-Ucp2), a protein known to uncouple mitochondrial membrane potential (Chakrabarty and Bhattacharyya, 2017). There was a substantial increase in the polysome-attached miRNA content in FH-Ucp2-expressing LDC stage cells (Fig. 2F). A high retention of miRNA with polysomes associated with retarded export of miRNAs from HDC state cells has been documented earlier in HDC cells; this was associated with low levels of EV or exosomal association of miRNAs (Ghosh et al., 2015). Increased stability of miRNAs observed in HDC state human cells is primarily caused by a retarded extracellular export of miRNAs together with increased miRNA retention with rER and polysomes. Like in HDC cells, expression of Ucp2 in LDC stage cells reduces the miRNA export via EVs (Fig. 2G).

Reconfirmation of mitochondrial abnormality-driven defective extracellular miRNA export was strengthened in subsequent experiments where mitochondria-defective ρ0 cells, an effective model to study neurodegenerative disease (Moreira et al., 2009), were used for measurement of miRNA activity and levels. As expected, we detected an increased cellular miRNA level in SH-SY5Y-ρ0 cells compared to that in the wild-type cells (Fig. 2H). The increased activity of miRISC observed was also consistent with increased cellular miRNA content (Fig. 2H). The increased miRNAs were found to be associated with Ago2 and polysomes (Fig. 2I,J), which was accompanied by a reduced export of miRNA let-7a in ρ0 cells (Fig. 2K). It has been observed previously that mitochondrial detethering from ER can also cause increased miRNAs levels in mammalian cells (Chakrabarty and Bhattacharyya, 2017). We observed similar loss in mitochondria–ER interaction in ρ0 cells (Fig. S3A,B). This observation is consistent with the idea that the mitochondrial detethering caused by mitochondrial depolarization in mammalian cells is responsible for the depolarization-associated effect on the cellular and exosomal miRNA content in HDC cells. Indeed, we also observed an expected decrease in mitochondria–ER interaction in HDC cells (Fig. 1D), which is consistent with the notion of mitochondrial depolarization-induced loss of ER and mitochondria contact (Chakrabarty and Bhattacharyya, 2017).

### Mitochondrial depolarization affects P-body targeting of Ago2 in human cells

Previous reports clearly enunciate elevated miRNA stability in human cells upon Ucp2 upregulation and reduction in $\Delta\Psi_M$ (Chakrabarty and Bhattacharyya, 2017). Moreover, the effect of $\Delta\Psi_M$ on Rck/p54 (also known as DDX6)-positive RNA processing body or P-bodies has been partly addressed in a previous study (Huang et al., 2011). Interestingly, impaired miRNA-mediated clearance of target RNA has been observed in HDC cells, with the target RNA, hence, being more stable than in proliferating cells (Ghosh et al., 2015). This is consistent with a reduced trafficking of the repressed mRNAs to P-bodies, where they may get degraded. In HDC cells, polysome sequestration of both miRNA and its target messages could account for the increased mRNA stability found in HDC or in cells with depolarized mitochondria. To discover the link between loss of $\Delta\Psi_M$ and P-body status, microscopic analyses were performed in cells treated with either FCCP or exogenously overexpressing FH-Ucp2, which causes disruption of mitochondrial membrane potential (Chakrabarty and Bhattacharyya, 2017). A distinct loss in visible Ago2-positive P-bodies was observed in cells treated with FCCP and in those expressing FH-Ucp2 (Fig. 3A,B). As expected, we also documented a reduced number of P-bodies in SH-SY5Y-ρ0 cells (Fig. S3C).

### Reduced P-body dynamics and Ago2 localization also happens in growth-retarded cells

Does impaired intracellular trafficking of miRNAs also result in defective P-body localization in HDC stage cells? There was

Journal of Cell Science (2020) 133, jcs250241. doi:10.1242/jcs.250241

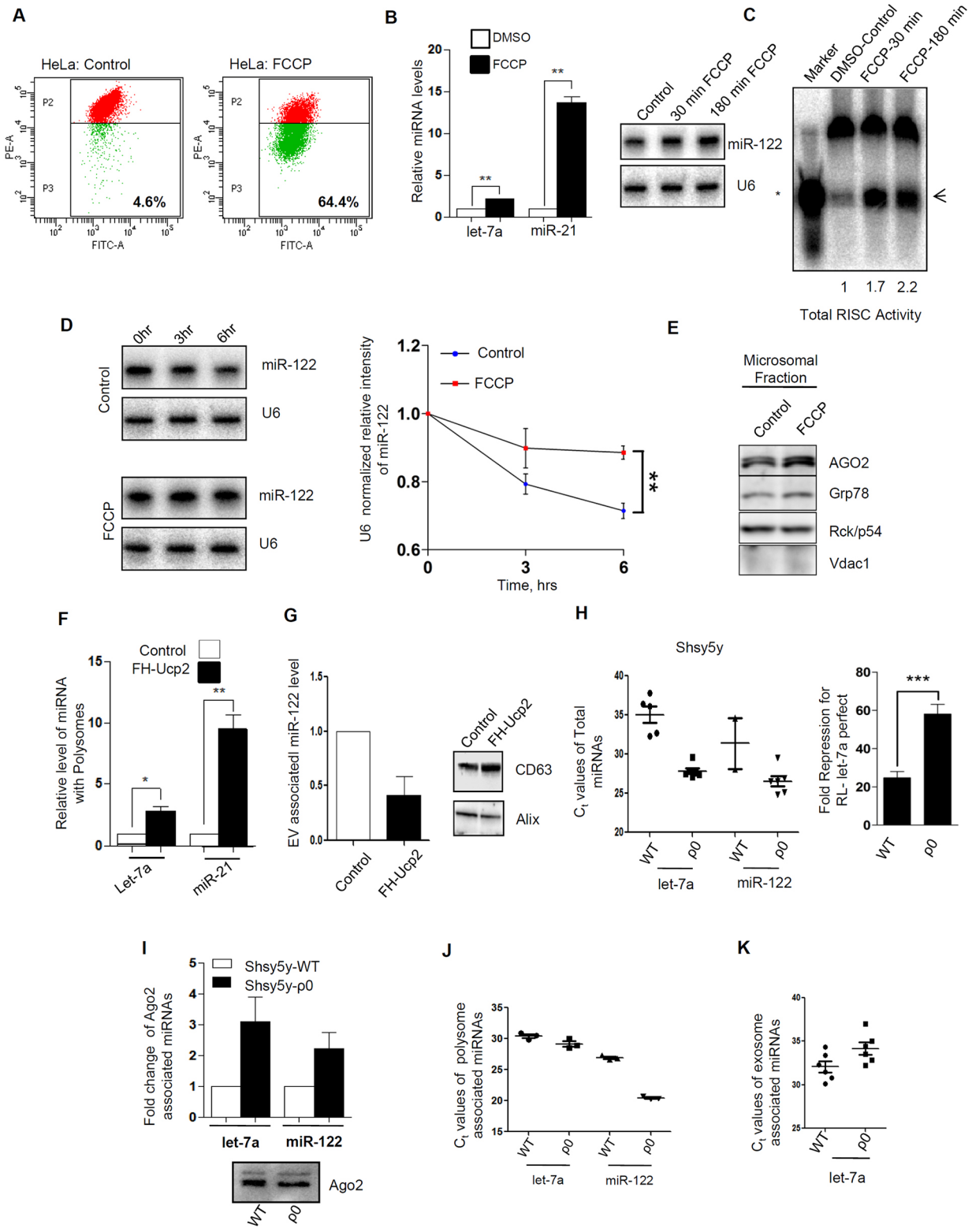


**Fig. 2.** See next page for legend.

a profound decrease in the number of visible Ago2 granules in HDC cells (Fig. 3C,D). We conducted immunofluorescence analysis of two established P-body components, Dcp1a and XRN1. In other cases, we used tagged versions of Dcp1a or Ago2 to track and document P-body status. To further probe the loss of distinct P-bodies with high cell confluency, HeLa cells were transfected with Myc–Ago2 and GFP–Dcp1a. Subsequently, these cells were co-immunostained with XRN1 to monitor the localization of Ago2 in such conditions. In LDC HeLa cells, most of the GFP–Dcp1a bodies were positive for Myc–Ago2 while in HDC cells Ago2



Journal of Cell Science

Journal of Cell Science (2020) 133, jcs250241. doi:10.1242/jcs.250241

**Fig. 2. Mitochondrial depolarization causes the microsomal accumulation of miRNPs and reduced exosomal export of miRNAs.** (A) Representative plots using flow cytometry-based quantification of JC-1 stained control or FCCP-treated HeLa cells. The percentage of cells in the zone of low JC-1 fluorescence (green) were measured and shown as depicted. (B) Levels of miR-21 and let-7a in FCCP-treated cells. The values were estimated by a qRT-PCR-based method in control and treated cells. Relative levels of miR-122 were estimated by northern blotting for HeLa cells treated with FCCP for indicated time periods (right panel). U6 was used as loading control for northern blots and used for normalization in qRT-PCR-based miRNA content quantifications. (C) Representative autoradiogram elucidating variation in RISC cleavage activity associated with Ago2 isolated from HeLa cells treated with FCCP for the indicated time periods. The *in vitro* RISC cleavage assay was performed with Ago2–miR-122 miRNPs isolated from HeLa cells treated with FCCP for the indicated time periods with an FH-Ago2 expression construct and pmiR-122, a miR-122 expression plasmid. The activities were measured and quantified in an *in vitro* RISC cleavage reaction using 5′-γ[$^{32}$P]-labeled miR-122 target RNA as substrate. Values below the blot indicate the relative RISC activity measured by estimating the cleaved band intensities (marked by arrowhead) against total amount of substrate used (uncleaved and cleaved RNA taken together) measured using densitometric analysis. Intensities were normalized to immunoprecipitated (IPed) FH-Ago2 levels. Asterisk indicates the position of a 21-nucleotide-long radiolabeled DNA oligonucleotide that was used as size marker. The immunoprecipitated FH-Ago2 intensities have been used for calculating specific activity RISC cleavage and depicted by the respective quantified values. (D) Mature miR-122 decay rate estimated by northern blotting (representative blot shown in the left panel) upon FCCP treatment for indicated time periods for HeLa cells. Band intensities from the northern blot for respective treatment times were normalized by U6 values and were used to plot the decay curve (right panel). Relative values (mean±s.e.m.) were plotted for the respective time points ($n$=3). (E) HeLa cells treated with FCCP or DMSO (control) for a time period of 3 h were used for the isolation of the total microsomal fraction by $CaCl_2$-based separation from crude microsomal fraction. Representative images of western blot analysis for indicated proteins from FCCP-treated microsomal fractions of HeLa cells. Absence of Vdac1 confirms the absence of mitochondrial contamination. (F) Polysomes from the cell extract were extracted. The relative enrichment of the miR-21 and let-7a within polysomal fractions are plotted (mean±s.e.m.) to determine the effect of Ucp2 expression on the polysomal miRNA level in mammalian cells. (G) qRT-PCR-based relative quantification of exogenously expressed miR-122 in EVs of HeLa cells expressing FH-Ucp2. Values were normalized against respective miRNA levels in control cells. Shown are the mean±s.e.m. from at least four independent experiments. A representative western blot analysis of exosomal marker CD-63 and Alix in the exosomal fraction of HeLa cells expressing FH-Ucp2 or control plasmid is shown on the right. Normalization was done against CD63 levels. (H) qRT-PCR based $C_t$ values of endogenous let-7a or exogenously introduced miR-122 levels in WT or ρ0 SH-SY5Y cells. In the right panel, *in vivo* let-7a miRNA activity in WT or ρ0 SH-SY5Y cells is shown. Relative repression level was measured by determining the *Renilla* luciferase luminescence in cells expressing luciferase-based let-7a reporter with one let-7a perfect site, RL-Con, a reporter without let-7a site was used as control. Shown are the mean±s.e.m. from at least three independent experiments. (I) Immunoprecipitation of endogenous Ago2 was performed to estimate changes in Ago2-associated miRNA levels of WT or ρ0 SH-SY5Y cells. Quantification was done by qRT-PCR-based estimation. Values (mean±s.e.m.) were normalized against amount of Ago2 immunoprecipitated and plotted against values of WT SH-SY5Y samples considered as unit. A representative blot showing immunoprecipitated endogenous Ago2 level used for normalization of respective miRNA levels. (J,K) qRT-PCR-based $C_t$ values of the polysomal fraction (J) or exosomal fraction (K) associated with endogenous let-7a or exogenously introduced miR-122 levels in WT or ρ0 SH-SY5Y cells. Shown are the mean±s.e.m. for $n$>3. *$P$<0.05, **$P$<0.01, ***$P$<0.001 (Student's $t$-test).

colocalization with GFP–Dcp1a was visibly reduced. Additionally, in HDC HeLa cells, the average number of discrete P-bodies was low (Fig. 3E,F).

P-body components are known to exchange their content with the cytosol, and most of the P-body markers are also ubiquitously found in the cytoplasm (Aizer et al., 2008). To ascertain whether the exchange dynamics of cargo is modulated in cells grown to confluent states, we performed fluorescence recovery after photobleaching (FRAP) analyses for the GFP-tagged P-body protein markers GFP–Dcp1a or GFP–Ago2. The majority of P-bodies in HDC and LDC HeLa cells, were found to be dynamically distinct although a similar recovery for GFP–Dcp1a to P-bodies was seen in both HDC and LDC cells. In contrast, recovery of GFP–Ago2 to P-bodies was reduced in HDC cells compared to LDC cells (Fig. S4A). The linear velocity and size of GFP–Ago2 positive P-bodies were distinctly higher in LDC than HDC HeLa cells (Fig. S4B,C).

### Restoration of mitochondrial potential rescues P-body numbers and intracellular miRNP shuttling

The $\Delta\Psi_M$-mediated effects upon P-body number, Ago2 localisation to P-bodies, polysomal sequestration of miRNAs and lowered miRNA export through EVs all occurs concurrently with a marked increase in Ucp2 protein levels. Moreover, many of these results were replicated in cells upon loss of $\Delta\Psi_M$ caused through chemical blocking of mitochondrial membrane potential, which induces a similar situation to that seen upon exogenous expression of Ucp2 in mammalian cells (Chakrabarty and Bhattcharyya, 2017). Therefore to specifically link Ucp2 upregulation with these effects on miRNP machineries and P-bodies observed in HDC cells, we used Genipin, which is a specific blocker of Ucp2 with an elevated level in HDC stage cells (Zhang et al., 2006). Successful restoration of $\Delta\Psi_M$ in HeLa HDC cells was observed post Genipin treatment (Fig. S5A). Moreover, Ago2-positive P-body numbers, as well as the Ago2 colocalization with Rck/p54 bodies, were partially restored upon Genipin treatment of HDC cells (Fig. S5B,C). This rescue in P-body number happened owing to a near complete reversal of Ucp2 protein levels in Genipin-treated HDC cells (Fig. S5D). Furthermore, both polysomal enrichment of miRNA and the lowered release of exosomal or EV-associated miRNAs from HDC cells were rescued to near LDC level upon specific blocking of Ucp2 (Fig. S5E,F). Hence, mitochondrial depolarization is directly linked with miRNA function, as well as its stability, and the elevation of Ucp2 protein level and function occurs in growth-retarded cells can be blocked by Genipin treatment to restore miRNA levels and P-body status.

### Mitochondrial detethering-induced retention of miRNPs on rER is caused by reduced rER targeting of eIF4E

Previous studies have shown that $\Delta\Psi_M$ regulates the mitochondria–ER tethering through the protein mitofusin 2 (Mfn2) (Schrepfer and Scorrano, 2016). Hence, we measured the cellular and polysomal association of miRNA and Ago2 protein in mouse embryonic fibroblasts with or without the Mfn2-encoding genes, to connect mitochondrial depolarization and detethering observed in HDC cells with reduced EV-mediated miRNA export. Interestingly, in the Mfn2 knockout cells we observed a substantial increase in polysome-associated miRNA and Ago2 protein with a concomitant decrease in exosomal miRNA content in EVs isolated from those cells (Fig. 4A–C).

What could cause the increased association of miRNPs with rER in Mfn2-negative cells? We observed a reduced amount of polysomes in Mfn2$^{-/-}$ cells (Fig. 4D). We checked the distribution of several translation initiation regulatory factors along with the elongation factor eEF2, and detected a specific loss of eIF4E, the very important cap-binding protein essential for translational initiation in the rER-associated fraction (Fig. 4E) (Sonenberg and Hinnebusch, 2009), although the cellular levels of

Journal of Cell Science (2020) 133, jcs250241. doi:10.1242/jcs.250241

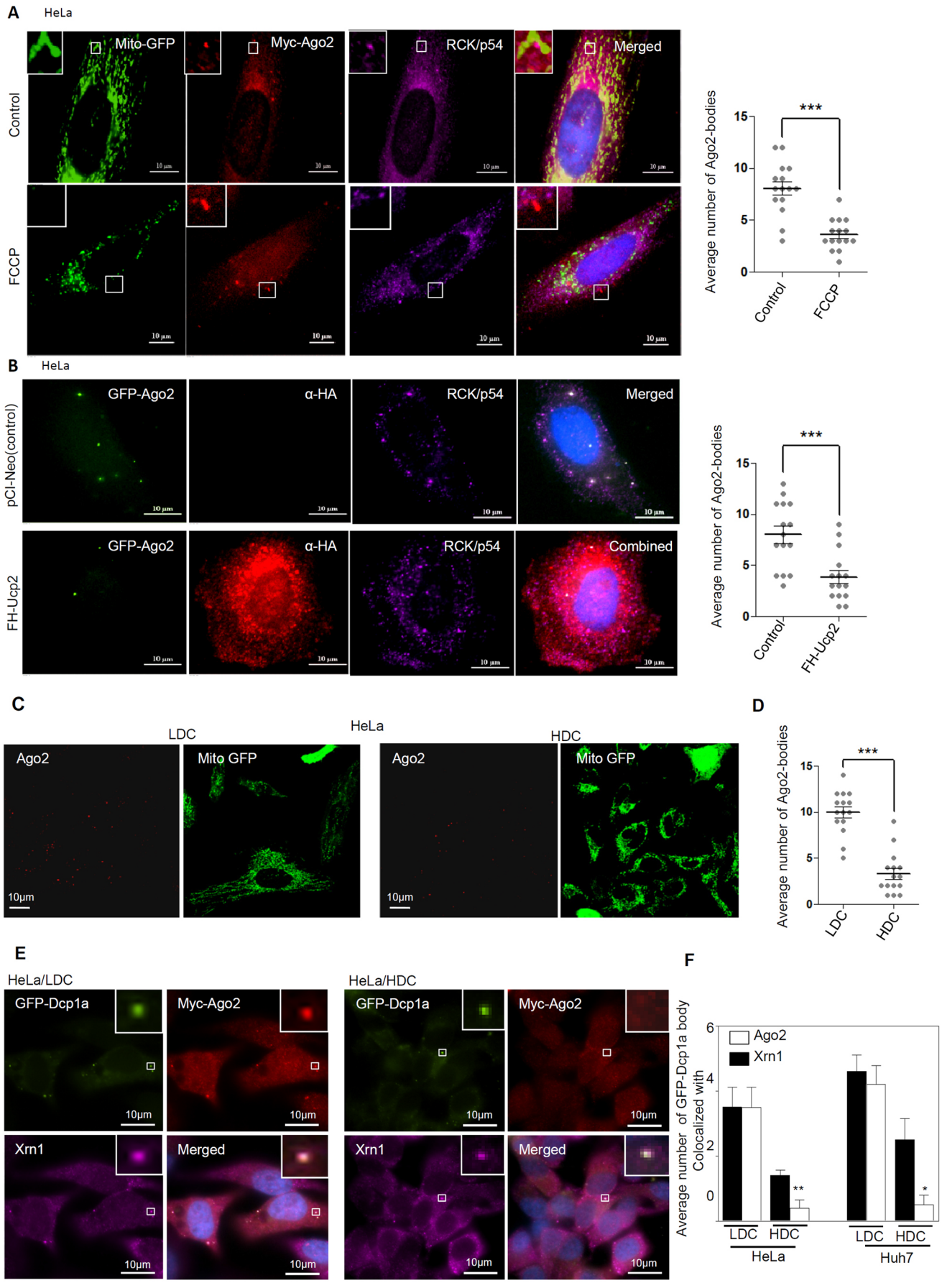


**Fig. 3.** See next page for legend.

Journal of Cell Science (2020) 133, jcs250241. doi:10.1242/jcs.250241

**Fig. 3. Effect of mitochondrial depolarization on P-bodies.** (A) FCCP treatment affects P-bodies. Representative frames of mitochondria in HeLa cells treated with FCCP. Cells expressing a mitochondrial targeting variant of GFP (Mito-GFP, green) and a Myc-tagged variant of Ago2 were used. Ago2 were labeled using anti-Myc (red) and antibodies against endogenous Rck/p54 (magenta) were used to label them by indirect immunofluorescence. DAPI was used for staining the nucleus. Scale bars: 10 µm. Quantification (mean±s.e.m.) of Myc–Ago2-positive bodies normalized to the number of cells (right). (B) Effect of Ucp2 expression on P-body status in HeLa cells. Representative frames of Ago2 in HeLa cells expressing FH-Ucp2. Cells expressing an Ago2 variant of GFP (Ago2–GFP, green) and FH-Ucp2 (red) were used. HA-Ucp2 was labeled using anti-HA and antibodies against endogenous Rck/p54 (magenta) were used to label P-bodies by indirect immunofluorescence. DAPI was used for depicting the nucleus. Scale bars: 10 µm. Quantification (mean±s.e.m.) of GFP–Ago2 bodies normalized to the number of cells (right). (C) Representative confocal microscopy frames showing mitochondria in HDC or LDC HeLa cells. Cells expressing a mitochondrial targeting variant of GFP (Mito-GFP, green) were used. Endogenous Ago2 was labeled via indirect immunofluorescence (red). (D) Estimation of Ago2 bodies was performed from frames shown in C and normalized to number of cells using Imaris. (E) Representative fluorescence microscopy frames of P-body markers in HDC or LDC HeLa cells. Cells expressing a GFP-tagged variant of Dcp1a (green) (GFP–Dcp1a) and a Myc-tagged variant of Ago2 (Myc–Ago2) were used. Anti-Myc antibody was used to detect Myc–Ago2 (red). Endogenous Xrn1 was detected using anti-human Xrn1 antibody (violet). DAPI staining was used to depict nuclei. (F) Estimation of Dcp1a bodies colocalizing with Xrn1 or Ago2 in HDC or LDC conditions of HeLa cell from frames as shown in a representative picture in E and normalized against number of cells. Shown are the mean± s.e.m from at least five independent experiments. *$P$<0.05, **$P$<0.01, ***$P$<0.001 (Student's $t$-test).

eIF4E remain unchanged in both wild-type and Mfn2$^{-/-}$ cells (Fig. 4E). Interestingly, in Mfn2$^{-/-}$ cells, eIF4E also showed an increased interaction with eIF4E-BP1, which may be due to an increased expression and decreased phosphorylation of eIF4E-BP1, ultimately causing an increase in its eIF4E binding in Mfn2$^{-/-}$ cells (Fig. 4E). The reduced recruitment of eIF4E to ER is consistent with the poor translation observed in Mfn2$^{-/-}$ cells, as revealed in the 15–35% sucrose density gradient analysis of cell extract for the components of protein translation machinery. Association of eIF4E with the heavier polysomal fraction was noted to be severely affected in Mfn2$^{-/-}$ cells compared to wild-type cells (Fig. 4F). KCl-puromycin treatment can extract attached polysomes from the ER membrane (Barman and Bhattacharyya, 2015). In subsequent experiments with KCl-puromycin, we found association of most of the translation initiation factors, including eIF4E, with the KCl-puromycin-soluble extract of translating polysomes attached to MEF-derived microsomes (Fig. 4G,H). This is consistent with previous observations that suggest microsome-attached membranes are the major site for translation regulation where the target message and miRNAs accumulate and interact, and mRNAs either get translated or repressed (Barman and Bhattacharyya, 2015). It has been shown previously that the low translatability of the mRNAs in HDC cells causes retention of the miRNPs with the rER-attached polysomes to cause increased miRNA stability, as effective translation is a pre-requisite for miRNP recycling (Ghosh et al., 2015). We also observed increased accumulation of target message and miRNA with the rER-attached polysomes in Mfn2-negative cells (Fig. 4I). Therefore, mitochondrial detethering of rER, which is also observed in HDC cells, may directly cause lowering of miRNA turnover by targeting the initiation phase of translation caused by poor shuttling of the cap-binding protein eIF4E from the cytoplasmic pool to the rER associated domain, a process controlled by its strong interaction with eIF4E-BP1, as observed in mitochondria-detethered cells. Interestingly the eIF4E-T (eIF4E-transporter; also known as EIF4ENIF1), a nuclear importer of eIF4E and a competitor of eIF4E-BP1 for eIF-4E binding, was also found to be predominantly absent in Mfn2$^{-/-}$ cells (Fig. 4E) (Dostie et al., 2000).

We wanted to study mTOR, the upstream regulatory kinase of eIF4E-BP1, to understand the regulatory cascade. We observed a relative decrease of cellular mTOR level in Mfn2$^{-/-}$ cells. This was also accompanied by a decrease in mTOR level in microsomes (normalized against calnexin, representing the total content of microsomes isolated upon the fractionation of MEF cells) (Fig. 4E). The level of phosphorylated S6K in the microsomal fraction was also decreased. Here, we could also observe increased phosphorylation of eIF2α, correlating with the defective translation status in Mfn2$^{-/-}$ cells (Fig. 4E). Increased phosphorylation of eIF2α has a profound effect on inactivation and downregulation of global protein synthesis inside the cells (Wengrod et al., 2015). To check whether phosphorylation of eIF2α is a manifestation of an activated unfolded protein response (UPR) pathway in Mfn2$^{-/-}$ MEF cells, we have checked activated PERK (also known as EIF2AK3) levels there. Although we could not find any difference on the total PERK expression, we could see increased p-PERK in Mfn2$^{-/-}$ MEF cells, which suggests a probable activated UPR response in Mfn2$^{-/-}$ MEFs (Fig. 4E).

To explore the possibility that PERK/UPR is connected to mTOR inactivation in Mfn2$^{-/-}$ MEF cells, we treated the wild-type MEF cells with UPR activator thapsigargin (TSG; 2.5 µM for 16 h) to determine the effect on mTOR signaling pathway. As also described in previous reports, we found inactivation of mTORC1 and its downstream molecules (Fig. S6A) (Preston and Hendershot, 2013). By contrast, no decreased microsomal compartmentalization of 4EBP1 was evident on TSG-treated cells. There was also no decrease in eIF4E or p-mTOR levels in the microsomal fraction of TSG-treated cells (Fig. S6B). Therefore, increased levels of p-PERK probably has no direct connection with the reduced microsomal targeting of eIF4E that has been noted in Mfn2$^{-/-}$ MEF cells.

### Reduced mTORC1 activity restricts the relocalization of eIF4E to rER

To prove the importance of eIF4E relocalization to polysomes in controlling miRNA stability in mammalian cells, we treated MDAM-MB-231 cells with rapamycin, an mTORC1 inhibitor (Sonenberg and Hinnebusch, 2009), and noted the reduction in mTORC1 phosphorylation and downstream activity as evident by the reduced 4EBP1 and S6K phosphorylation seen in rapamycin-treated cells (Fig. 5A). This was consistent with a reduction in the level of eIF4E-BP1 phosphorylation and relocalization of eIF4E to rER fraction (Fig. 5A). With a reduction in eIF4E location to rER or microsomes, we documented an increase in miRNA content both in total and polysome-associated pools upon rapamycin treatment (Fig. 5B,C). Like in HDC or HA–Ucp2-expressing cells, rapamycin treatment also resulted in a lower number of P-bodies in treated cells (Fig. 5D).

To further scrutinize the role of mTORC1 in eIF4E recruitment and miRNA metabolism, we activated the mTOR signaling pathway in HDC cells by expressing Myc–Rheb, a constitutive activator of mTORC1, which is known to act upstream of mTOR and activate the pathway (Inoki et al., 2003). We could correlate the Rheb-mediated activation of downstream pathway, where increased mTORC1 level leads to increased phosphorylation of its downstream substrates, with increased microsomal and polysomal compartmentalization of eIF4E (Fig. S6F,G). Also, we observed reduced polysomal sequestration of miRNAs in these conditions, suggesting an active intracellular trafficking of miRNPs in high Rheb and activated mTORC1 conditions (Fig. S6H–J). The

Journal of Cell Science (2020) 133, jcs250241. doi:10.1242/jcs.250241

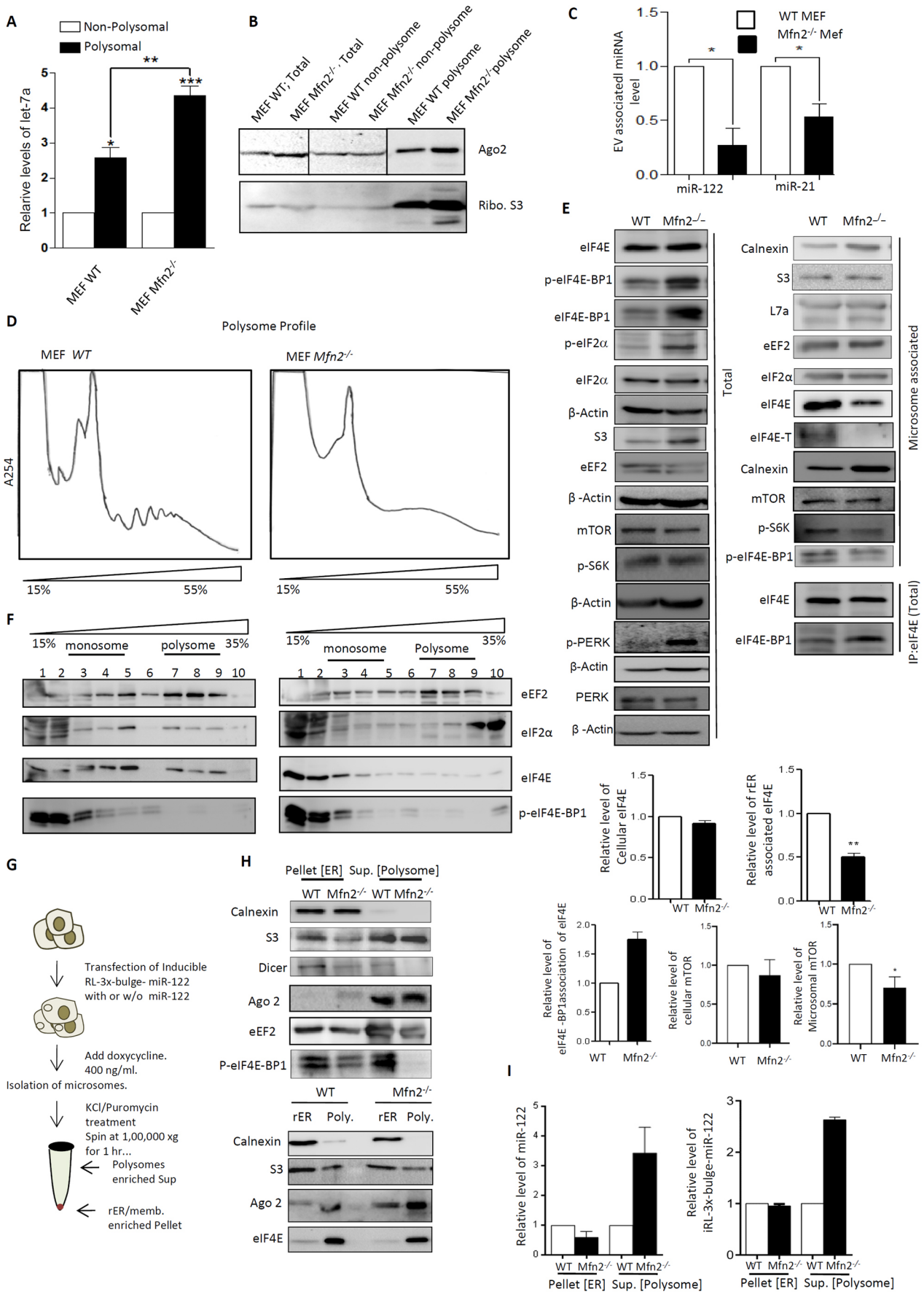


**Fig. 4.** See next page for legend.

Journal of Cell Science (2020) 133, jcs250241. doi:10.1242/jcs.250241

**Fig. 4. Defective targeting of eIF4E to rER-attached polysomes causes retarded intracellular miRNA trafficking and export.** (A) qRT-PCR-based relative quantification of endogenous let-7a levels in polysomal and non-polysomal fractions obtained from a one-step polysome separation done with MEFs of indicated genotypes. Values were normalized against U6 RNA and relative miRNA levels are shown. Values are the mean±s.e.m. from at least four independent experiments. (B) Representative western blot analysis of Ago2 in total extract or polysomal and non-polysomal fractions after one-step polysome separation done with MEFs of indicated genotypes. For comparison between cells of different genotypes, equal amounts of proteins were loaded, while for comparison between subcellular fractions a cell equivalent amount of each fraction was analyzed. Ribosomal S3 marks the presence of ribosomes, and is enriched in the polysomal fraction. (C) qRT-PCR-based relative quantification of exogenously expressed miR-122 or endogenous miR-21 levels in extracellular vesicles (EVs) derived from MEFs of the indicated genotypes. Individual values were normalized against protein content of the EVs and relative values between cell types are shown. Values are the mean±s.e.m. from at least four independent experiments. (D) Cell extracts from WT and Mfn2$^{-/-}$ MEFs were isolated and analyzed on a 15–55% sucrose density gradient. Gradient fractions were further collected and absorbance was monitored at 254 nm and the respective absorbance profile graphs were plotted. (E) Relative abundance of different translation factors (eIF4E, p-eIF4E-BP1, p-eIF2α, eEF2 and eIF2α), mTOR or ribosomal protein S3, PERK and p-PERK in cell extracts and microsomes derived from MEF WT and MEF Mfn2$^{-/-}$ cells. Total or microsomal fractions were analyzed by western blotting. β-Actin and calnexin were internal controls for cellular and microsomal samples, respectively. Endogenous cellular eIF4E was immunoprecipitated and association of eIF4E-BP1 with immunoprecipitated materials was analyzed by western blotting in WT and Mfn2$^{-/-}$ MEF extracts. Relative quantification of eIF4E in individual fractions or its interaction with eIF4E-BP1 was quantified by densitometric analysis of western blot data from multiple experiments. Relative mTOR levels in total and microsomal fractions were also quantified. (F) Extracts of MEFs (WT and Mfn2$^{-/-}$) were isolated and analyzed on a 15–35% sucrose density gradient, and different fractions were collected and proteins were isolated. Distribution profile of different translation factors (eEF2, eIF2α, eIF4E and p-eIF4E-BP1) were analyzed by western blots. (G) Schematic representation of KCl-puromycin-based extraction method for isolation of polysomes attached with the microsomal membrane from MEFs. (H) Microsomes from WT or Mfn2$^{-/-}$ MEFs were treated with KCl-puromycin to extract the translating polysomes. Furthermore, proteins and RNAs were isolated from residual ER and solubilized polysome-enriched fractions. Samples were analyzed by western blotting to check distribution of miRNP proteins (Ago2 and Dicer) and translation factors after the extraction. The respective distribution of the ER and ribosomal marker proteins (calnexin and S3) were also checked and were followed to ensure proper fractionation in H. (I) Amount of miRNAs and mRNAs were also quantified by qRT-PCR-based quantification against U6 or ribosomal RNA content. Shown are the mean ± s.e.m. for $n$>3. *$P$<0.05, **$P$<0.01, ***$P$<0.001 (Student's $t$-test).

observations in LDC cells or in Rheb-overexpressing conditions suggest the *de facto* crucial role of mTORC1 to mediate the mitochondrial polarization-driven compartmentalization of eIF4E, which ultimately decides the fate of miRNAs and target mRNAs.

We undertook experiments in HDC and LDC cells to score the levels of p-mTOR and eIF4E, and noted a decrease on p-mTOR content along with eIF-4E levels in HDC cells (Fig. 5E). For isolated microsomes or rER, we observed a reduction of eIF4E content in HDC cells microsomes along with reduced p-mTOR levels (Fig. 5F). Similar lowering of cellular and microsomal eIF4E was also noted in cells expressing FH-Ucp2 (Fig. 5E,F). Therefore, reduced mTORC1 activity is responsible for reduced phosphorylation of eIF4E-BP1 and free eIF4E required for miRNA trafficking and export in HDC cells. Similar decrease of microsome-associated mTOR was also noted in cells depleted for Mfn2 (Fig. 4E).

Interestingly, we found that there was an increased p-AMPK level in the total and microsomal fraction in HDC cells (Fig. S6C). To verify whether AMPK plays a more prominent role than the mTOR pathway, we went on to inhibit the AMPK activation pathway in HDC cells to see the concurrent effect on differential rER targeting of translational factors. Compound C (or dorsomorphin) is known conventionally to inhibit AMPK pathway activation (Zhou et al., 2001). Previous reports and our observations collectively suggest that there is increased mTORC1 activation after Compound C treatment of MDA-MB-231 cells in HDC conditions (Fig. S6D) (Ng et al., 2012). We could not observe restoration of translation factor localization in Compound C-treated HDC cells, but we did see reduced p-mTOR and eIF4E enrichment on microsomes compared to in the untreated control (Fig. S6E). These observations suggest that there are different modes of AMPK-mediated inactivation of mTORC1, which is probably a separate phenomenon to that mediated by mTOR and eIF4E localization to rER. Therefore, AMPK deactivation is likely uncoupled with mTORC1 and eIF4E localization to polysomes or microsomes in LDC cells. AMPK probably is not part of the mTORC1-mediated regulatory network for differential compartmentalization of eIF4E that we are reporting in our defective mitochondrial context (Ucp2-overexpressing or Mfn2$^{-/-}$ cells).

## DISCUSSION

The incorporation of eIF4E into the eIF4F translation initiation complex is reciprocally controlled through a family of inhibitor proteins, called the eIF4E-binding proteins (4E-BPs). eIF-4E mediates the attachment of eIF4F with the 5′-cap structure of the mRNA to initiate cap-dependent translation in the cytoplasm. Presence of phosphorylated mTOR (i.e. activated mTORC1) on rER membrane probably triggers eIF4E-BP1 phosphorylation and thus increasing the amount of free eIF4E available to promote translation of microsome-attached miRNA-repressed mRNAs to increase intracellular miRNA trafficking and export. In cells with defective mitochondrial conditions or treated with an inhibitor, mTOR cannot get properly activated, which resulted in decreased rER-mediated migration of eIF-4E, which leads to reduced translation and increased stability and poor intracellular shuttling of mRNAs and the cognate miRNAs (Fig. 6).

Recent reports define mitochondria, along with ER, as the key players in miRNA activity regulation (Barman and Bhattacharyya, 2015; Bose et al., 2017; Stalder et al., 2013). Mitochondrial control of miRNA function and stability are primarily controlled by Ucp2 and Mfn2. Ucp2 alters the $\Delta\Psi_M$ and affects tethering between mitochondria and ER, which, in turn, is essential for the association and interaction between ER and endosomes. This association is evidently important for the transfer of target RNA-loaded miRISC from ER, the site of miRISC–target RNA interaction, to endosomes and MVBs, where miRISC uncoupling and target RNA degradation occurs (Bose et al., 2017; Chakrabarty and Bhattacharyya, 2017). Elevation of Ucp2 protein levels causes increased uncoupling of mitochondria, which results in a cascade of events including defective interaction between these membranes. Moreover, polysomal miRISC interaction is known to be dependent on translational speed and efficiency (Ghosh et al., 2015). Thus, mitochondria might be a key player in protein translation as a potential supplier of localized ATP and, hence, act as a determinant, even during the earlier steps in miRISC nucleation process, by modulating global translational rate (Bose et al., 2020).

The increased stabilities of both miRNAs and their target messages were caused by their retention with translationally 'inactive' polysomes attached with rER membrane in HDC cells (Ghosh et al., 2015). The importance of m7G cap-binding of mRNA

Journal of Cell Science (2020) 133, jcs250241. doi:10.1242/jcs.250241

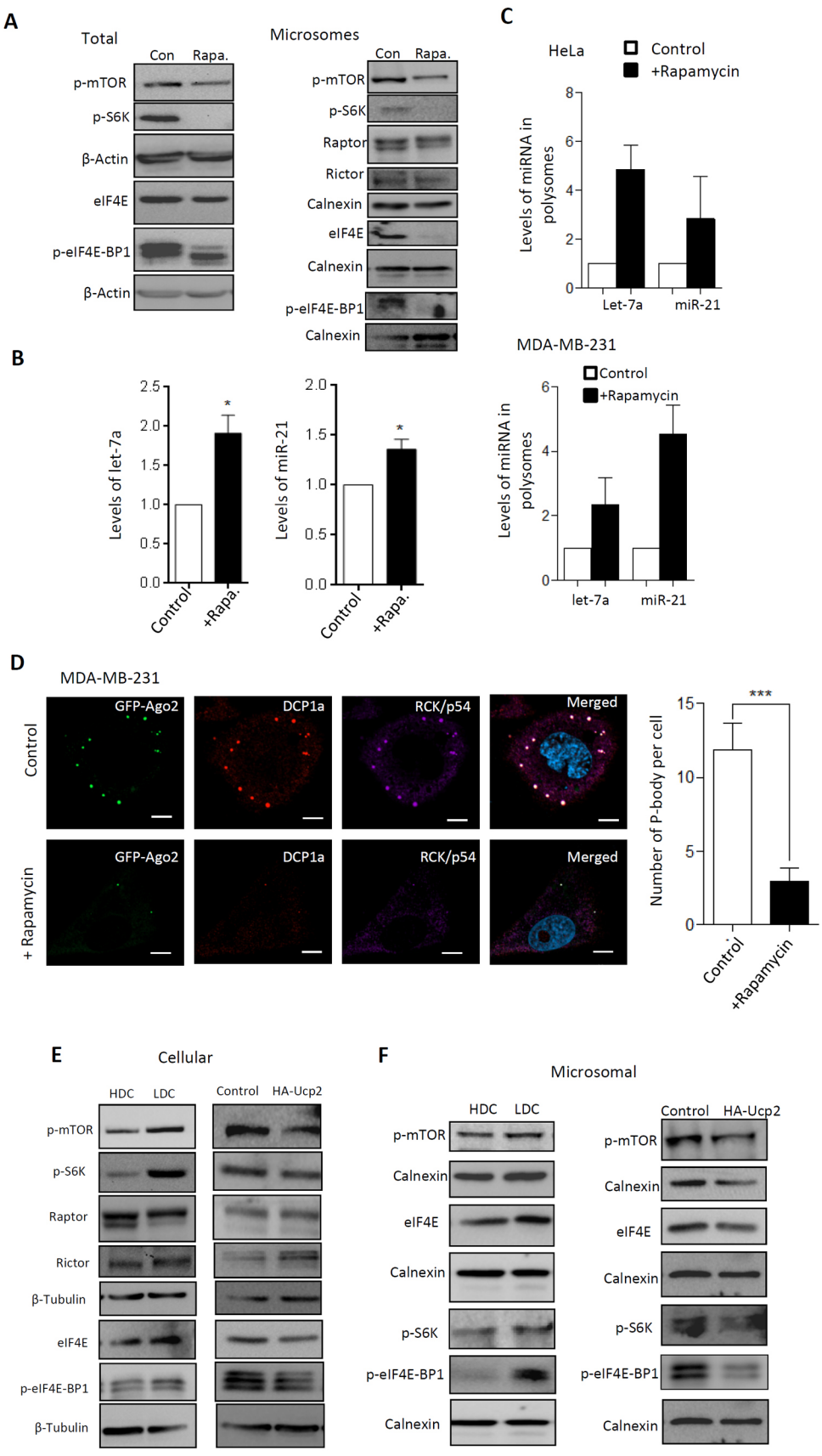


**Fig. 5. mTORC1 drives polysomal compartmentalization of eIF4E in mammalian cells to accelerate miRNA export.** (A) Cellular and microsomal distribution of different translation factors (eIF4E, p-eIF4E-BP1 and p-S6K) and mTOR complex proteins (p-mTOR, Raptor and Rictor) after 16 h of 100 nM rapamycin or control (DMSO) treatment in MDAM-MB-231 cells. Protein samples from total or microsomal fractions were analyzed by western blotting. β-Actin and calnexin were used as loading controls for total and microsomal fractions, respectively. (B) Quantitative RT-PCR data to check cellular let-7a and miR-21 levels after 16 h of 100 nM rapamycin treatment compared to control (DMSO-treated) MDAM-MB-231 cells. U6 snRNA served as an internal control. (C) Quantitative RT-PCR data shows let-7a and miR-21 levels on polysomal fractions after 16 h of 100 nM Rapamycin treatment compared to control (no Rapamycin) of MDAM-MB-231 cells. U6 snRNA was used for normalization. In B,C values are mean±s.d. from three biological replicates. (D) Representative confocal microscopy images showing P-bodies in untreated control or 100 nM rapamycin-treated MDA-MB-231 cells. Cells expressing an Ago2 variant of GFP (Ago2–GFP, green) were used for treatment. Antibodies against endogenous Rck/p54 (magenta) and Dcp1a (red) were used to label P-bodies by indirect immunofluorescence. DAPI was used for depicting the nuclei. Scale bars: 10 µm. Quantification of number of P-bodies, normalized to the number of cells was done for untreated control or rapamycin-treated MDA-MB-231 cells as shown in the representative image obtained (right). (E) Expression of mTORC1, eIF4E, phopshorylated S6K and eIF4E-BP1 in LDC and HDC MDAM-MB-231 cells. β-Tubulin was used for normalization. (F) Levels of translational initiation factor eIF4E and phosphorylated mTOR for microsomes isolated from HDC or LDC cells and also in HA-Ucp2 cells compared to vector control-transfected cells. Amount of microsomes used for analysis were evident from the calnexin levels in individual fraction. *$P$<0.05, ***$P$<0.001 (paired two-tailed Student's $t$-test).

by eIF4E and its recruitment to mRNAs is a prerequisite for continuous production of proteins from respective mRNAs. In previous papers, eIF4E recruitment has been shown as one the highly regulated steps in eukaryotic translation control (Filipowicz and Sonenberg, 2015), and recruitment of some specific inhibitory factors, such as eIF4E-T, is even regulated indirectly by miRNPs

Journal of Cell Science (2020) 133, jcs250241. doi:10.1242/jcs.250241

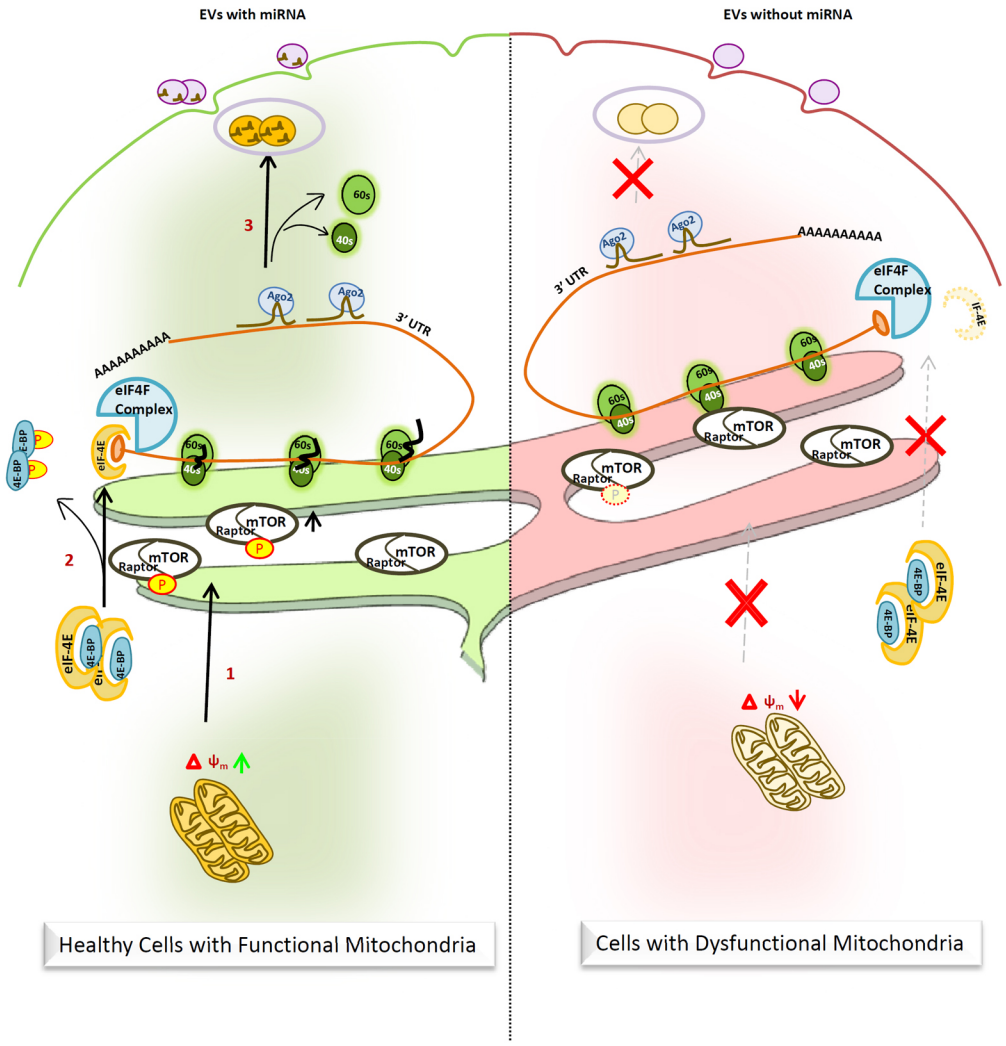


**Fig. 6. A schematic representation of how mitochondria-controlled differential activation of mTOR governs intracellular trafficking and extracellular export of miRNAs in mammalian cells.** Mammalian cells with functional mitochondria show proper activation of mTOR, which leads to subsequent migration and phosphorylation of 4E-BPs on polysomes attached to rER, dissociation of inactive eIF-4Es and its recruitment onto the active eIF4F translation initiation complex. This follows proper intracellular shuttling and extracellular export of miRNAs and dissociation of ribosomal subunits for another set of new cycles. The process gets impaired in cells containing defective mitochondria (depolarized or detethered from rER).

bound to cis-acting elements on the 3′UTR of the same mRNAs (Filipowicz and Sonenberg, 2015).

In HDC cells, mRNAs with miRNA-binding sites are repressed in a m7G-Cap structure-dependent manner. As per our hypothesis, stimulation of miRNA-repressed messages happens due to high availability of eIF4E, as its interactor protein eIF4E-BP gets phosphorylated in the LDC cells. This eventually increases intracellular movement of mRNA and miRNA in a manner linked to high miRNA export. Therefore, it mimics the situation that happens with 5′TOP element-containing mRNAs, translation of which is stalled due to the repression in low translation conditions (Thoreen et al., 2012). mTORC1 upregulation more specifically promotes the translation of TOP element-containing translationally inactive mRNAs over non-TOP mRNA.

The role of the P-bodies as the degradation sites of mRNA and the mechanisms relevant to a particular context is an essential, yet difficult to answer problem, because the underlying networks are large, complex and only partially understood. Since the disassembly of large P-bodies during high density of growth does not completely abrogate mRNA decay (Ghosh et al., 2015), it remains to be explored whether P-body function can be sufficiently backed up by microscopically invisible small-sized PBs (that may be unaltered in HDC state cells). Deployment of mRNAs from the translation machineries by a miRNA-repressive action is considered a prerequisite for P-body localization of miRNP-targeted mRNAs. Maybe this process of spatial aggregation reduces the energetic burden on the cell by lowering the overall entropy of the system. Our study reveals interesting changes in cellular P-body numbers and dynamics in response to environmental cues originating from cell–cell contact and modulated by the cellular energy landscape that is primarily governed by mitochondrial functionality and status.

The ER–endosome association, an interaction regulated through Ucp2-mediated perturbation of mitochondrial membrane potential, is defective in growth-retarded cells due to an elevation in Ucp2 protein level. This results in a loss of association between the pools of miRNPs present on ER and endosomes in growth-retarded cells, and causes a subsequent rise in polysomal miRNA content with reduced P-body targeting of miRNP components like Ago protein. Moreover, a concurrent decrease in the miRNA content of extracellular vesicles was observed in both mitochondria compromised and HDC cells. Furthermore, Ucp2-driven alteration in organelle interaction modulates miRNA activity and therefore Ucp2 can potentially act as a key regulator of various cell fate determinant processes.

Mitochondria under classical starvation conditions exhibit a more proliferative nature and an upregulated networking incidence (Rambold et al., 2011). But for cells in the HDC state, we found that impaired fission or fusion events could be directly attributed to the increased uncoupling of oxidative phosphorylation and the electron transport chain due to upregulation of the uncoupling protein Ucp2 in the HDC state. The specific difference between a

Journal of Cell Science (2020) 133, jcs250241. doi:10.1242/jcs.250241

starved cell and cells under HDC condition is the variability of oxygen utilization rather than the oxygen consumption rate, as HDC cells have a tendency to undergo more futile cycles of oxidative phosphorylation. This is due to leaky proton channels caused by significantly higher expression of uncoupling proteins in comparison to regular amino acid/glucose starvation instances. Other reports have also shown that the Ucp2 might have different roles and can even tilt the metabolic balance towards increased oxidative phosphorylation instead of glycolysis in some cancer cells (Esteves et al., 2014). The overall idea thus indicates a vital involvement of Ucp2, in this case differentiating it from the outcomes of nutrient starvation of cells. Additionally, the senescent nature of the cells in HDC state has also been shown previously (Ghosh et al., 2015) and it is known that senescent cells can show higher oxygen consumption (Hubackova et al., 2019). Therefore, the high oxygen consumption in HDC cells is well explained.

UPR or Mfn2 loss differs in their effect on eIF4E compartmentalization. Phosphorylation of eIF2α probably occurs through activated PERK-mediated pathways, and we assume a crosstalk of the mTOR pathway with the UPR pathway may aggravate the change that we are observing in Mfn2-negative cells. Altogether, the data suggests that defective mitochondria tethering of rER caused by Mfn2 loss-of-function probably plays a crucial role to reduce rER targeting of eIF4E, with an activated UPR response playing an additive role by specifically upregulating eIF2α phosphorylation and by generally decreasing the translation process of all mRNAs irrespective of their miRNA-mediated repression or not. We propose that in the translationally defective condition the upregulated eIF4E may more specifically work on already repressed mRNAs by miRNAs and these mRNAs 'win over' otherwise non-repressed mRNAs. The increase in phosphorylated eIF2α level causes an overall slow down in translation process. However, UPR activation alone could not elicit the reported observation, as eIF4E could not get transferred to rER.

Overall, mitochondria, by regulating the organellular dynamics and inter-organelle exchange of materials, play a key role in controlling miRNP redistribution in a process heavily regulated by both intrinsic and extrinsic cues, such as availability of nutrients and growth factors.

## MATERIALS AND METHODS

### Cell culture and treatment

HeLa, MDA-MB-231, MEFs, SH-SY5Y (obtained from the ATCC) and Huh7 cells (a gift from Witold Filipowicz, Friedrich Miescher Institute for Biomedical Research, Basel, Switzerland) were grown in Dulbecco's modified Eagle's medium (DMEM) with 2 mM L-glutamine and supplemented with 10% heat-inactivated fetal calf serum (FCS). Cell were regularly monitored for any contamination microscopically. For all experiments, cells were grown to 25–40% confluency states (LDC) or visibly full confluent (HDC) states unless specified otherwise (Ghosh et al., 2015). Transfections were performed using Lipofectamine 2000 (Invitrogen) following the manufacturer's protocol. FCCP (500 nM) treatment was performed for the indicated times. Genipin and rapamycin were used at 100 µM and 100 nM concentrations, respectively (Chakrabarty and Bhattacharyya, 2017). Thapsigargin and dorsomorphin were used at 2.5 µM and 10 µM concentration on MEF and MDAM-MB-231 cells, respectively (Chakraborty et al., 2019; Mukherjee et al., 2016). For Rheb overexpression experiments, MDAM-MB-231 cells were transfected with Myc-tagged Rheb overexpression plasmids and after 48 h of transfection further analysis was undertaken (Tyagi et al., 2015).

### Immunofluorescence

For immunofluorescence, cells grown on six-well tissue culture plate were transfected with 250 ng of GFP–Ago2, GFP–Dcp1a or N-HA-GW182 encoding plasmids (Pillai et al., 2005). The cells were split after 24 h of transfection and subjected to specific experimental conditions. For immunofluorescence analysis, cells were fixed with 4% paraformaldehyde for 30 min, permeabilized and blocked with PBS containing 1% BSA and 0.1% Triton X-100 and 10% goat serum (GIBCO) for 30 min. After incubation with primary antibodies in the same buffer at desired dilution (see Table S1) overnight at 4°C and subsequent washing steps, secondary anti-rabbit or anti-mouse-IgG antibodies labeled with Alexa Fluor® 488 dye (green), Alexa Fluor® 594 dye (red) or Alexa Fluor® 647 dye (far red) fluorochromes (Molecular Probes) were used at 1:500 dilutions. After 2 h of incubation at 37°C for 1 h followed by washing steps, cells were mounted with Vectashield with DAPI (Vector Labs) and observed under a Plan Apo VC 60×/1.40 oil or Plan Fluor 10×/0.30 objectives on an inverted Eclipse Ti Nikon microscope equipped with a Nikon Qi1MC or QImaging-Rolera EMC$^2$ camera for image capture. A few images were taken also on Zeiss Confocal Imager LSM800.

For live-cell analysis, 250 ng of GFP–Ago2 or GFP–Dcp1a-encoding plasmid was used for transfection of cells grown in a six-well plate. For FRAP experiments, cells were photo bleached, and recovery was monitored for a total duration of less than 4 min. Glass bottom Petri dishes pre-coated with gelatin were used for cell growth for live-cell imaging. Cells were observed with a 60×/N.A.1.42 Plan Apo N objective. Images were captured with an IXON3 EMCCD camera in an ANDOR Spinning Disc Confocal Imaging System on an Olympus IX81 inverted microscope. All images were captured on Nikon Eclipse Ti microscope or ANDOR spinning disc microscope was processed with Nikon NIS ELEMENT AR 3.1 software. P-body tracking and velocity calculations were performed with IMARISx64 software developed by BITPLANE AG Scientific software. All velocities were calibrated against the net velocity of the cell boundary. In FRAP experiments, the intensities of the photobleached regions were recorded. The net intensity value at each time interval was normalized to the intensity of the same region before photobleaching and expressed as a percentage of the initial intensity for plotting. The intensity at the time of photobleaching was set to 0 for comparison of different sets of data.

### RNA isolation and real-time PCR

RNA was extracted with Trizol (Invitrogen) as per the manufacturer's protocol followed by DNase I treatment (Invitrogen) to remove residual DNA contamination. Real-time analyses by two-step RT-PCR was performed for quantification of miRNA on a 7500 real-time PCR system (Applied Biosystems) or Bio-Rad CFX96™ real time system using an Applied Biosystems Taqman chemistry-based miRNA assay system.

miRNA assays were performed using specific primers for human let-7a (assay ID 000377), human miR-122 (assay ID 000445), human miR-21 (assay ID 000397). U6 snRNA (assay ID 001973) was used as an endogenous control. One third of the reverse transcription mix was subjected to PCR amplification with TaqMan® Universal PCR Master Mix No AmpErase (Applied Biosystems) and the respective TaqMan® reagents for target miRNA. Samples were analyzed in triplicate from a minimum of three biological replicates. The comparative $C_t$ method which typically included normalization by the U6 snRNA for each sample was used for all instances. For mRNA quantification, a Eurogentec Reverse Transcriptase Core Kit was used to prepare cDNA from RNA sample. Real-time (reverse transcriptase) PCR from cDNA was performed with the Mesa Green qPCR Mastermix Plus for SYBR Assay-Low ROX (Eurogentec). 18 s rRNA was used as endogenous control.

### Western blotting and luciferase assay

Western blot analyses of different miRNP components (Ago2, RCK/p54 and XRN1) and other various associated regulatory factors were performed as described previously (Ghosh et al., 2015). A detailed list of antibodies used is available as Table S1. Imaging of all western blots was performed using an UVP BioImager 600 system equipped with Vision Works Life Science software (UVP) V6.80. Dual luciferase reporter assays were been performed using a Dual-Luciferase Assay Kit (Promega), as per the manufacturer's instructions, on a VICTOR X3 Plate Reader (PerkinElmer). Renilla luciferase (RL) luminescence was normalized using Firefly luciferase (FF) activities to calculate the relative fold repression.

Journal of Cell Science (2020) 133, jcs250241. doi:10.1242/jcs.250241

### Microsome isolation

For microsome isolation, cells were resuspended in 1× hypotonic buffer (10 mM HEPES pH 7.8, 1 mM EGTA and 25 mM KCl) equivalent to three times the packed cell volume (PCV) and incubated for 20 min on ice. The cells were spun down and resuspended in 2 volumes of 1× isotonic buffer (10 mM HEPES pH 7.8, 1 mM EGTA, 25 mM KCl and 250 mM sucrose) and homogenized manually. Post pre-clearing of cell debris and unlysed cells was undertaken by centrifugation at 1000 ***g*** for 10 min; the mitochondrial fraction was removed by centrifugation at 12,000 ***g*** for 15 min. The post-mitochondrial supernatant was incubated for 15 min with 8 mM $CaCl_2$ followed by centrifugation at 8000 ***g*** for 10 min to isolate the microsomal pellet. The detailed protocol is described elsewhere (Barman and Bhattacharyya, 2015). The isolation of polysomes from microsomes by KCl-puromycin treatment was performed as described elsewhere (Barman and Bhattacharyya, 2015; Bose et al., 2017).

### OptiPrep density gradient-based fractionation of cellular organelles

For cell fractionation in an iodixanol gradient (OptiPrep® gradient), roughly $2\times10^7$ cells were used. The cell pellet incubated in a hypotonic buffer (50 mM HEPES pH 7.8, 78 mM KCl, 4 mM $MgCl_2$, 8.4 mM $CaCl_2$, 10 mM EGTA, 250 mM sucrose, 100 µg/ml cycloheximide, 5 mM vanadyl ribonucleoside complex, and 1× EDTA-free protease inhibitor cocktail) was homogenized by 30–40 strokes in a glass Dounce homogenizer (Sartorius). The cell homogenate was cleared by centrifugation at 1000 ***g*** twice, and the cleared supernatant was loaded on a 3 to 30% iodixanol gradient (OptiPrep) and ultracentrifuged for 5 h at 36,000 rpm in an SW60 rotor (Beckman Coulter). Fractions were collected manually through aspiration, and RNA or proteins were isolated for further analysis.

### Sucrose density gradient-based fractionation of polysomes

For polysome analysis, $\sim2\times10^7$ cells, grown to the desired level of confluency, were lysed in a buffer containing 10 mM HEPES pH 8.0, 25 mM KCl, 5 mM $MgCl_2$, 1 mM DTT, 5 mM vanadyl ribonucleoside complex, 1% Triton X-100, 1% sodium deoxycholate and 1× EDTA-free protease inhibitor cocktail (Roche) supplemented with 100 µg/ml cycloheximide. Polysome profiles were obtained by measuring the absorbance at 254 nm using ISCO UA-6 absorbance monitor and fractions were collected on ISCO gradient fractionator. RNA and proteins were isolated from each individual fraction and analyzed.

### Single-step polysome isolation

For one-step polysome isolation, cells were lysed in a buffer containing 10 mM HEPES, pH 8.0, 25 mM KCl, 5 mM $MgCl_2$, 1 mM DTT, 5 mM vanadyl ribonucleoside complex, 1% Triton X-100, 1% sodium deoxycholate, and 1X EDTA-free protease inhibitor cocktail (Roche) supplemented with 100 µg/ml cycloheximide. Lysates were cleared by spinning at 3000 ***g*** followed by 20,000 ***g*** for 10 min each and supernatant were loaded on a 30% sucrose cushion and spun for 1 h at 31,200 rpm in SW60 rotor (Beckman Coulter). The non-polysomal supernatant was removed, and polysomes collected below the sucrose layer was diluted with the hypotonic buffer (10 mM HEPES pH 7.8, 25 mM KCl, 5 mM $MgCl_2$, 1 mM DTT) and spun for another 30 min at the same speed. The supernatant was removed and polysome pellet was re-suspended in hypotonic buffer mentioned above.

### Flow cytometry-based mitochondrial membrane potential estimation

JC-1 dye (Life Technologies), a mitochondrial membrane potential-sensitive probe (Life Technologies) was used to label cells according to the manufacturer's protocol. Cells were harvested and incubated with 1 mM of JC-1 in the culture medium for 15 mins at 37°C in presence of 5% $CO_2$. Cells were then harvested and washed with 1× PBS and analyzed on a BD FACS CALIBUR instrument following the manufacturer's protocol.

### Measurement of mitochondrial oxygen consumption

HeLa and MDA-MB-231 cells were plated accordingly as low (50% confluency) and high (100% confluency) density cultures in 24-well cell plates (Seahorse Bioscience) in DMEM containing 10% FBS and placed in a 5% $CO_2$ incubator. On the following day, DMEM base medium (Seahorse Bioscience, North Billerica, MA, USA) was supplemented with 25 µM D-glucose, and 1 µM sodium pyruvate (adjusted to pH 7.4) was added to the cells and incubated for 1 h in a non-$CO_2$ incubator at 37°C. The three injections ports (A–C) of the XFe cartridge were loaded with oligomycin (Oligo, 1 µM), carbonyl cyanide-4-trifluoromethoxyphenylhydrazone (FCCP, 0.5 µM), and rotenone and antimycin A (Rot+Anti A, 1 µM), respectively, followed by equilibration and calibration in the instrument for 12 min. Following this, the cell plate was loaded to initiate measurement of oxygen consumption rate (OCR) following a 3 min wait, 2 min mix and 3 min measure cycle over a total period of ∼1 h. Protein estimation was performed by ELISA using Bradford's reagent to normalize the obtained OCR values; the OCR was expressed in pmol/min/mg protein.

### *In vitro* RISC cleavage assay

*In vitro* RISC cleavage assay with affinity-purified miRISC-122 was carried out using a 36 nt RNA 5′-AAAUUCAAACACCAUUGUCACACUCCA-CCAGAUUAA-3′ bearing the sequence complementary to mature miR-122. The reaction was carried out in a total volume of 30 µl with 10 fmol of 5′ γ[$^{32}$P]-labeled RNA in buffer (100 mM KCl, 5.75 mM $MgCl_2$, 2.5 mM ATP and 0.5 mM GTP) and the protein equivalent amount of RISC at 30°C for 30 min. After RNA isolation, products were electrophoresed on a 12% denaturing 8 M Urea–PAGE gel and visualized by autoradiography.

### Extracellular vesicle or exosome purification and treatments

A standard purification procedure for EVs or exosomes was based on differential ultracentrifugation. The first steps were designed to eliminate large dead cells and large cell debris by successive centrifugations at increasing speeds. The cleared, conditioned medium was centrifuged for 20 min at 2000 ***g***, 4°C. Subsequently the supernatant was pipetted off and centrifuged for 30 min at 10,000 ***g***, 4°C. Careful removal of all the supernatant was ensured such that none of the pellet contaminated the supernatant. The residual supernatant was subjected to a single filtration step using a 0.22 µm filter. This eliminated any residual dead cells and large debris while keeping small membranes intact for further purification by ultracentrifugation. The collected supernatant was gently layered over a 2 M sucrose cushion and subsequently centrifuged for at least 70 min at 100,000 ***g***, 4°C. Post ultracentrifugation the supernatant over the sucrose cushion level was gently removed by aspiration. The remaining volume containing exosomes was diluted in 1× PBS and centrifuged for at least 30 min at 100,000 ***g***, 4°C. The pellet obtained was resuspended in each tube in 1 ml PBS, using a micropipette. The resuspended pellet in PBS was centrifuged for 1 h at 100,000 ***g***, 4°C. To resuspend the final pellet (i.e. exosomes), a small volume of PBS or passive lysis buffer (PLB) was added. To avoid contamination from exosomes present in serum used in the culture medium, exosome pre-cleared serum was used to grow the cells for exosome measurement experiments. The protocols were followed as described previously (Basu and Bhattacharyya, 2014; Ghosh et al., 2015; Mukherjee et al., 2016).

### Post imaging analysis and others

All western blot images were processed with Adobe Photoshop CS4 for all linear adjustments and cropping. All images captured on Nikon Eclipse Ti microscope or ANDOR spinning disc microscope were processed with Nikon NIS ELEMENT AR 3.1 software. P-body tracking and velocity calculations were performed with IMARISx64 software developed by BITPLANE AG Scientific software. Image cropping was done using Adobe Photoshop CS4. All graphs and statistical analyses were generated in GraphPad Prism 5.00 (GraphPad, San Diego, CA). A two-sample Student's *t*-test was used for analysis. $P<0.05$ was considered to be statistically significant and >0.05 were not significant (ns). Error bars indicate mean±s.e.m.

#### Acknowledgements

We acknowledge Witold Filipowicz, Sanjay Ghosh, Krishna Das Saha and Subhas C. Biswas for different plasmid constructs, reagents and antibodies.

#### Competing interests

The authors declare no competing or financial interests.

**Author contributions**
Conceptualization: S.C., Y.C., S.B., S.G., S.N.B.; Methodology: S.C., Y.C., S.B., S.N.B.; Software: Y.C., S.B., S.G.; Validation: Y.C., S.G.; Formal analysis: S.G., S.N.B.; Investigation: S.C., Y.C., S.B., S.G.; Data curation: S.C., S.N.B.; Writing - original draft: S.N.B.; Visualization: S.N.B.; Supervision: S.N.B.; Project administration: S.N.B.; Funding acquisition: S.N.B.

**Funding**
S.N.B. is supported by The Swarnajayanti Fellowship (SJF/LS-03/2014-15) from Department of Scientific and Industrial Research, Ministry of Science and Technology, India, while Y.C., S.B., S.C. and S.G. received their support from Council of Scientific and Industrial Research, India (CSIR). We are supported by funds from High Risk High Reward Project Grant (HRR/2016/00093), Science and Engineering Research Board, Dept. of Science and Technology, Govt. of India and an Indo-French Centre for the Promotion of Advanced Research (CEFIPRA) Project Grant (6003-J).

**Supplementary information**
Supplementary information available online at
https://jcs.biologists.org/lookup/doi/10.1242/jcs.250241.supplemental

**Peer review history**
The peer review history is available online at
https://jcs.biologists.org/lookup/doi/10.1242/jcs.250241.reviewer-comments.pdf

**References**

**Aizer, A., Brody, Y., Ler, L. W., Sonenberg, N., Singer, R. H. and Shav-Tal, Y.** (2008). The dynamics of mammalian P body transport, assembly, and disassembly in vivo. *Mol. Biol. Cell* **19**, 4154-4166. doi:10.1091/mbc.e08-05-0513

**Barman, B. and Bhattacharyya, S. N.** (2015). mRNA Targeting to endoplasmic reticulum precedes ago protein interaction and MicroRNA (miRNA)-mediated translation repression in mammalian cells. *J. Biol. Chem.* **290**, 24650-24656. doi:10.1074/jbc.C115.661868

**Bartel, D. P.** (2009). MicroRNAs: target recognition and regulatory functions. *Cell* **136**, 215-233. doi:10.1016/j.cell.2009.01.002

**Basu, S. and Bhattacharyya, S. N.** (2014). Insulin-like growth factor-1 prevents miR-122 production in neighbouring cells to curtail its intercellular transfer to ensure proliferation of human hepatoma cells. *Nucleic Acids Res.* **42**, 7170-7185. doi:10.1093/nar/gku346

**Bhattacharyya, S. N., Habermacher, R., Martine, U., Closs, E. I. and Filipowicz, W.** (2006). Relief of microRNA-mediated translational repression in human cells subjected to stress. *Cell* **125**, 1111-1124. doi:10.1016/j.cell.2006.04.031

**Bose, M., Barman, B., Goswami, A. and Bhattacharyya, S. N.** (2017). Spatio-temporal uncoupling of miRNA-mediated translational repression and target RNA degradation controls miRNP recycling in mammalian cells. *Mol. Cell. Biol.* **37**, e00464-16. doi:10.1128/MCB.00464-16

**Bose, M., Chatterjee, S., Chakrabarty, Y., Barman, B. and Bhattacharyya, S. N.** (2020). Retrograde trafficking of Argonaute 2 acts as a rate-limiting step for de novo miRNP formation on endoplasmic reticulum-attached polysomes in mammalian cells. *Life Sci. Alliance* **3**, e201800161. doi:10.26508/lsa.201800161

**Brand, M. D., and Nicholls, D. G.** (2011). Assessing mitochondrial dysfunction in cells. *Biochem. J.* **435**, 297–312. doi:10.1042/BJ20110162

**Chakrabarty, Y. and Bhattacharyya, S. N.** (2017). Leishmania donovani restricts mitochondrial dynamics to enhance miRNP stability and target RNA repression in host macrophages. *Mol. Biol. Cell* **28**, 2091-2105. doi:10.1091/mbc.e16-06-0388

**Chakraborty, S., Datta, S. and Ghosh, S.** (2019). Induction of autophagy under nitrosative stress: A complex regulatory interplay between SIRT1 and AMPK in MCF7 cells. *Cell. Signal.* **64**, 109411. doi:10.1016/j.cellsig.2019.109411

**Dostie, J., Ferraiuolo, M., Pause, A., Adam, S. A. and Sonenberg, N.** (2000). A novel shuttling protein, 4E-T, mediates the nuclear import of the mRNA 5′ cap-binding protein, eIF4E. *EMBO J.* **19**, 3142-3156. doi:10.1093/emboj/19.12.3142

**Ernoult-Lange, M., Benard, M., Kress, M. and Weil, D.** (2012). P-bodies and mitochondria: which place in RNA interference? *Biochimie* **94**, 1572-1577. doi:10.1016/j.biochi.2012.03.008

**Esteves, P., Pecqueur, C., Ransy, C., Esnous, C., Lenoir, V., Bouillaud, F., Bulteau, A. L., Lombes, A., Prip-Buus, C., Ricquier, D. et al.** (2014). Mitochondrial retrograde signaling mediated by UCP2 inhibits cancer cell proliferation and tumorigenesis. *Cancer Res.* **74**, 3971-3982. doi:10.1158/0008-5472.CAN-13-3383

**Eulalio, A., Behm-Ansmant, I., Schweizer, D. and Izaurralde, E.** (2007). P-body formation is a consequence, not the cause, of RNA-mediated gene silencing. *Mol. Cell. Biol.* **27**, 3970-3981. doi:10.1128/MCB.00128-07

**Filipowicz, W. and Sonenberg, N.** (2015). The long unfinished march towards understanding microRNA-mediated repression. *RNA* **21**, 519-524. doi:10.1261/rna.051219.115

**Ghosh, S., Bose, M., Ray, A. and Bhattacharyya, S. N.** (2015). Polysome arrest restricts miRNA turnover by preventing exosomal export of miRNA in growth-retarded mammalian cells. *Mol. Biol. Cell* **26**, 1072-1083. doi:10.1091/mbc.E14-11-1521

**Gibbings, D. J., Ciaudo, C., Erhardt, M. and Voinnet, O.** (2009). Multivesicular bodies associate with components of miRNA effector complexes and modulate miRNA activity. *Nat. Cell Biol.* **11**, 1143-1149. doi:10.1038/ncb1929

**Huang, L., Mollet, S., Souquere, S., Le Roy, F., Ernoult-Lange, M., Pierron, G., Dautry, F. and Weil, D.** (2011). Mitochondria associate with P-bodies and modulate microRNA-mediated RNA interference. *J. Biol. Chem.* **286**, 24219-24230. doi:10.1074/jbc.M111.240259

**Hubackova, S., Davidova, E., Rohlenova, K., Stursa, J., Werner, L., Andera, L., Dong, L., Terp, M. G., Hodny, Z., Ditzel, H. J. et al.** (2019). Selective elimination of senescent cells by mitochondrial targeting is regulated by ANT2. *Cell Death Differ.* **26**, 276-290. doi:10.1038/s41418-018-0118-3

**Hubstenberger, A., Courel, M., Benard, M., Souquere, S., Ernoult-Lange, M., Chouaib, R., Yi, Z., Morlot, J. B., Munier, A., Fradet, M. et al.** (2017). P-Body purification reveals the condensation of repressed mRNA regulons. *Mol. Cell* **68**, 144-157.e5. doi:10.1016/j.molcel.2017.09.003

**Hunter, M. P., Ismail, N., Zhang, X., Aguda, B. D., Lee, E. J., Yu, L., Xiao, T., Schafer, J., Lee, M.-L. T., Schmittgen, T. D. et al.** (2008). Detection of microRNA expression in human peripheral blood microvesicles. *PLoS ONE* **3**, e3694. doi:10.1371/journal.pone.0003694

**Inoki, K., Li, Y., Xu, T. and Guan, K. L.** (2003). Rheb GTPase is a direct target of TSC2 GAP activity and regulates mTOR signaling. *Genes Dev.* **17**, 1829-1834. doi:10.1101/gad.1110003

**Labbé, K., Murley, A. and Nunnari, J.** (2014). Determinants and functions of mitochondrial behavior. *Annu. Rev. Cell Dev. Biol.* **30**, 357-391. doi:10.1146/annurev-cellbio-101011-155756

**Li, S., Liu, L., Zhuang, X., Yu, Y., Liu, X., Cui, X., Ji, L., Pan, Z., Cao, X., Mo, B. et al.** (2013). MicroRNAs inhibit the translation of target mRNAs on the endoplasmic reticulum in Arabidopsis. *Cell* **153**, 562-574. doi:10.1016/j.cell.2013.04.005

**Moreira, P. I., Cardoso, S. M., Pereira, C. M., Santos, M. S. and Oliveira, C. R.** (2009). Mitochondria as a therapeutic target in Alzheimer's disease and diabetes. *CNS Neurol. Disord. Drug Targets* **8**, 492-511. doi:10.2174/187152709789824651

**Morita, M., Gravel, S.-P., Chénard, V., Sikström, K., Zheng, L., Alain, T., Gandin, V., Avizonis, D., Arguello, M., Zakaria, C. et al.** (2013). mTORC1 controls mitochondrial activity and biogenesis through 4E-BP-dependent translational regulation. *Cell Metab.* **18**, 698-711. doi:10.1016/j.cmet.2013.10.001

**Mukherjee, K., Ghoshal, B., Ghosh, S., Chakrabarty, Y., Shwetha, S., Das, S. and Bhattacharyya, S. N.** (2016). Reversible HuR-microRNA binding controls extracellular export of miR-122 and augments stress response. *EMBO Rep.* **17**, 1184-1203. doi:10.15252/embr.201541930

**Ng, T. L., Leprivier, G., Robertson, M. D., Chow, C., Martin, M. J., Laderoute, K. R., Davicioni, E., Triche, T. J. and Sorensen, P. H. B.** (2012). The AMPK stress response pathway mediates anoikis resistance through inhibition of mTOR and suppression of protein synthesis. *Cell Death Differ.* **19**, 501-510. doi:10.1038/cdd.2011.119

**Parker, R. and Sheth, U.** (2007). P bodies and the control of mRNA translation and degradation. *Mol. Cell* **25**, 635-646. doi:10.1016/j.molcel.2007.02.011

**Pillai, R. S., Bhattacharyya, S. N., Artus, C. G., Zoller, T., Cougot, N., Basyuk, E., Bertrand, E. and Filipowicz, W.** (2005). Inhibition of translational initiation by Let-7 MicroRNA in human cells. *Science* **309**, 1573-1576. doi:10.1126/science.1115079

**Preston, A. M. and Hendershot, L. M.** (2013). Examination of a second node of translational control in the unfolded protein response. *J. Cell Sci.* **126**, 4253-4261. doi:10.1242/jcs.130336

**Ramanathan, A. and Schreiber, S. L.** (2009). Direct control of mitochondrial function by mTOR. *Proc. Natl. Acad. Sci. USA* **106**, 22229-22232. doi:10.1073/pnas.0912074106

**Rambold, A. S., Kostelecky, B., Elia, N. and Lippincott-Schwartz, J.** (2011). Tubular network formation protects mitochondria from autophagosomal degradation during nutrient starvation. *Proc. Natl. Acad. Sci. USA* **108**, 10190-10195. doi:10.1073/pnas.1107402108

**Schrepfer, E. and Scorrano, L.** (2016). Mitofusins, from mitochondria to metabolism. *Mol. Cell* **61**, 683-694. doi:10.1016/j.molcel.2016.02.022

**Simons, M. and Raposo, G.** (2009). Exosomes–vesicular carriers for intercellular communication. *Curr. Opin. Cell Biol.* **21**, 575-581. doi:10.1016/j.ceb.2009.03.007

**Sonenberg, N. and Hinnebusch, A. G.** (2009). Regulation of translation initiation in eukaryotes: mechanisms and biological targets. *Cell* **136**, 731-745. doi:10.1016/j.cell.2009.01.042

**Stalder, L., Heusermann, W., Sokol, L., Trojer, D., Wirz, J., Hean, J., Fritzsche, A., Aeschimann, F., Pfanzagl, V., Basselet, P. et al.** (2013). The rough endoplasmatic reticulum is a central nucleation site of siRNA-mediated RNA silencing. *EMBO J.* **32**, 1115-1127. doi:10.1038/emboj.2013.52

**Théry, C., Zitvogel, L. and Amigorena, S.** (2002). Exosomes: composition, biogenesis and function. *Nat. Rev. Immunol.* **2**, 569-579. doi:10.1038/nri855

**Thoreen, C. C., Chantranupong, L., Keys, H. R., Wang, T., Gray, N. S. and Sabatini, D. M.** (2012). A unifying model for mTORC1-mediated regulation of mRNA translation. *Nature* **485**, 109-113. doi:10.1038/nature11083

**Tyagi, R., Shahani, N., Gorgen, L., Ferretti, M., Pryor, W., Chen, P. Y., Swarnkar, S., Worley, P. F., Karbstein, K., Snyder, S. H. et al.** (2015). Rheb inhibits protein synthesis by activating the PERK-eIF2alpha signaling cascade. *Cell Rep* **10**, 684-693. doi:10.1016/j.celrep.2015.01.014

**Valadi, H., Ekström, K., Bossios, A., Sjöstrand, M., Lee, J. J. and Lötvall, J. O.** (2007). Exosome-mediated transfer of mRNAs and microRNAs is a novel mechanism of genetic exchange between cells. *Nat. Cell Biol.* **9**, 654-659. doi:10.1038/ncb1596

**van Niel, G., D'Angelo, G. and Raposo, G.** (2018). Shedding light on the cell biology of extracellular vesicles. *Nat. Rev. Mol. Cell Biol.* **19**, 213-228. doi:10.1038/nrm.2017.125

**Wengrod, J., Wang, D., Weiss, S., Zhong, H., Osman, I. and Gardner, L. B.** (2015). Phosphorylation of eIF2alpha triggered by mTORC1 inhibition and PP6C activation is required for autophagy and is aberrant in PP6C-mutated melanoma. *Sci. Signal.* **8**, ra27. doi:10.1126/scisignal.aaa0899

**Zhang, C. Y., Parton, L. E., Ye, C. P., Krauss, S., Shen, R., Lin, C. T., Porco, J. A. Jr and Lowell, B. B.** (2006). Genipin inhibits UCP2-mediated proton leak and acutely reverses obesity- and high glucose-induced beta cell dysfunction in isolated pancreatic islets. *Cell Metab* **3**, 417-27. doi:10.1016/j.cmet.2006.04.010

**Zhou, G., Myers, R., Li, Y., Chen, Y., Shen, X., Fenyk-Melody, J., Wu, M., Ventre, J., Doebber, T., Fujii, N. et al.** (2001). Role of AMP-activated protein kinase in mechanism of metformin action. *J. Clin. Invest.* **108**, 1167-1174. doi:10.1172/JCI13505